On the dwarf irregular galaxy NGC 6822. I. Young, intermediate and old stellar populations.

Maria Tantalo ![ORCID],[1,2] Massimo Dall'Ora,[3] Giuseppe Bono,[1,2] Peter B. Stetson,[4] Michele Fabrizio,[2,5] Ivan Ferraro,[2] Mario Nonino,[6] Vittorio F. Braga,[2,5,7] Ronaldo da Silva,[2,5] Giuliana Fiorentino,[2] Giacinto Iannicola,[2] Massimo Marengo,[8] Matteo Monelli,[7,9] Joseph P. Mullen,[8] Adriano Pietrinferni,[10] and Maurizio Salaris[11,10]

[1]Dipartimento di Fisica, Università di Roma Tor Vergata, via della Ricerca Scientifica 1, 00133 Roma, Italy
[2]INAF - Osservatorio Astronomico di Roma, via Frascati 33, 00078 Monte Porzio Catone, Italy
[3]INAF - Osservatorio Astronomico di Capodimonte, Salita Moiariello 16, 80131 Napoli, Italy
[4]Herzberg Astronomy and Astrophysics, National Research Council, 5071 West Saanich Road, Victoria, British Columbia V9E 2E7, Canada
[5]Space Science Data Center, via del Politecnico snc, 00133 Roma, Italy
[6]INAF – Osservatorio Astronomico di Trieste, Via G. B. Tiepolo 11, 34143 Trieste, Italy
[7]Instituto de Astrofísica de Canarias, Calle Via Lactea s/n, E-38205 La Laguna, Tenerife, Spain
[8]Department of Physics and Astronomy, Iowa State University, Ames, IA 50011, USA
[9]Departamento de Astrofísica, Universidad de La Laguna (ULL), E-38200, La Laguna, Tenerife, Spain
[10]INAF - Osservatorio Astronomico d'Abruzzo, via M. Maggini, s/n, I-64100, Teramo, Italy
[11]Astrophysics Research Institute, Liverpool John Moores University, 146 Brownlow Hill, Liverpool L3 5RF, United Kingdom

ABSTRACT

We present accurate and deep multi-band (g, r, i) photometry of the Local Group dwarf irregular galaxy NGC 6822. The images were collected with wide field cameras at 2m/4m- (INT,CTIO,CFHT) and 8m-class telescopes (SUBARU) covering a 2 square degrees FoV across the center of the galaxy. We performed PSF photometry of $\approx$7,000 CCD images and the final catalog includes more than 1 million objects. We developed a new approach to identify candidate field and galaxy stars, and performed a new estimate of the galaxy center by using old stellar tracers finding that it differs by 1.15 (RA) and 1.53 (DEC) arcmin from previous estimates. We also found that young (Main Sequence, Red Supergiants), intermediate (Red Clump, Asymptotic Giant Branch [AGB]) and old (Red Giant Branch [RGB]) stars display different radial distributions. Old stellar population is spherically distributed and extends to radial distances larger than previously estimated ($\sim$1 degree). The young population shows a well defined bar and a disk-like distribution, as suggested by radio measurements, that is off-center compared with old population. We discuss pros and cons of the different diagnostics adopted to identify AGB stars and develop new ones based on optical-NIR-MIR color-color diagrams (CCDs) to characterize Oxygen and Carbon (C) rich stars. We found a mean population ratio between Carbon and M-type (C/M) stars of 0.67±0.08 (optical/NIR/MIR) and we used the observed C/M ratio with empirical C/M-metallicity relations to estimate a mean iron abundance of [Fe/H]$\sim$-1.25 (σ=0.04 dex) that agrees quite well with literature estimates.

Keywords: Dwarf irregular galaxies(417) — Stellar photometry(1620) — Stellar populations(1622) — Asymptotic giant branch stars(2100) — Metallicity(1031)

1. INTRODUCTION

Stellar systems hosting stellar populations ranging from very young (a few Myr) main sequence stars to old (t>10 Gyr) low-mass stars are rare in the Local Group (LG). The most prominent systems, but the three large LG galaxies (Milky Way [MW], M31, M33), are the Magellanic Clouds (MCs). However, we still lack firm theoretical and empirical constraints of their mutual dynamical interaction and of their interaction with the MW. This means that the star formation episodes

Corresponding author: Maria Tantalo
maria.tantalo@students.uniroma2.eu, maria.tantalo@inaf.it

and their chemical enrichment histories might have been either affected or driven by the environment. The three next stellar systems sharing similar metallicity distributions and hosting Wolf Rayet stars are the three LG dwarf irregulars IC 10, IC 1613 and NGC 6822 (Neugent & Massey 2019). These three systems are considered unique analogs of star forming galaxies observed at high redshift and populating the universe at the peak of cosmic star formation history (Stott et al. 2013; Du et al. 2020).

NGC 6822 brings forward several key properties that make this stellar system particularly interesting (key positional, structural and photometric properties are listed in Table 1). a) The position on the sky ($\alpha_{1950} = 19^h42^m04^s.2$, $\delta_{1950} = -14^\circ 56'24''$; Gottesman & Weliachew 1977) is such that it can be observed from both the northern and the southern hemisphere. b) The true distance modulus based on the Tip of the Red Giant Branch (TRGB) is $\mu = 23.54 \pm 0.05$ mag (Lee, Freedman & Madore 1993; Fusco et al. 2012) that agree quite well with similar estimates based on different standard candles (classical Cepheids: Gieren et al. 2006; Madore et al. 2009; Feast et al. 2012; Rich et al. 2014; Mira variables: Whitelock et al. 2013; carbon stars: Parada et al. 2021). The reddening shows a clumpy distribution and the current estimates show a broad variety when moving from the region close to the galaxy center (E(B-V) $\sim$ 0.45 mag) to the outermost (E(B-V) $\sim$ 0.25 mag) regions (Massey et al. 1995; Gallart, Aparicio & Vilchez 1996; Gieren et al. 2006; Cannon et al. 2006; Fusco et al. 2012). This means that NGC 6822 is a factor of two closer in distance and less affected by differential reddening when compared with IC 10. c) The metallicity distribution based on medium resolution spectra shows a well defined peak located at [Fe/H]= -1.05 ± 0.01 and a standard deviation of σ= 0.49 dex (Kirby et al. 2013). This measurement suggests that its mean chemical composition is, within the errors, quite similar to IC 1613 ([Fe/H]= -1.19 ± 0.01, σ = 0.37 dex). However, this iron abundance refers to the old stellar population in NGC 6822. Metallicity measurements for young stellar population have also been widely investigated. From the spectra of two A-type supergiants Venn et al. (2001) found a mean iron abundance of [Fe/H]= -0.49 ± 0.22, while Lee et al. (2006) obtained a mean oxygen abundance of [O/H]= -0.55 from optical spectra of five HII regions. More recently, Patrick et al. (2015) found a mean metallicity of [Z]= -0.52 ± 0.21 by using medium-resolution near-IR spectra of eleven red supergiants (RSGs). The difference in metallicity between old and young stellar populations and the possible presence of a metallicity gradient in the innermost

Table 1. Positional, structural and photometric properties of NGC 6822.

Parameter		Ref.[a]
α (J1950)[b]	$19^h42^m04^s.2$	[1]
δ (J1950)[b]	$-14^\circ 56'24''$	[1]
R_{half} (')[c]	16.13 ± 0.5^n	[2]
r_t (')[d]	40 ± 10	[3]
θ (°)[e]	62	[2]
ϵ [f]	0.35	[2]
V (mag)[g]	8.1 ± 0.2	[4]
M_V (mag)[h]	-15.2 ± 0.2	[5]
$(m-M)_0$ (mag)[i]	23.38 ± 0.04	[6]
$E(B-V)$ (mag)[j]	0.35 ± 0.04	[6]
$[Fe/H]$[k]	-1.05 ± 0.01	[7]
$[Z]$[l]	-0.52 ± 0.21	[8]
$[O/H]$[m]	-0.55	[9]

NOTE—[a] [1] Gottesman & Weliachew (1977); [2] Zhang, Mackey & Da Costa (2021); [3] Hodge et al. (1991); [4] Dale et al. (2007); [5] McConnachie (2012) [6] Rich et al. (2014); [7] Kirby et al. (2013); [8] Patrick et al. (2015); [9] Lee et al. (2006). [b] Galaxy center based on neutral hydrogen radio measurements. [c] Half-light radius. [d] Truncation radius. [e] Position angle. [f] Eccentricity. [g] Apparent visual magnitude. [h] Absolute visual magnitude. [i] True distance modulus. [j] Color excess. [k] Mean iron abundance of the old population. [l] Mean metallicity of the young population. [m] Mean oxygen abundance of HII regions. [n] The R_{half} value was obtained by using the relation $R_{half} = 1.68r_0$ (Martin, de Jong & Rix 2008) under the assumption of an exponential density profile and with the scale length provided by Zhang et al. (2021, $r_0 = 9.6 \pm 0.3'$).

galaxy regions were explained by Patrick et al. (2015) using a closed-box chemical evolution model. This model is based on plane physical arguments and takes account for the increase in the mean metallicity when moving from old to young stellar populations. However, NGC 6822 has a complex morphology, larger samples of old and young stellar tracers and more detailed chemical evolution models are required to constrain its chemical enrichment history. The measurements of the α-element abundances are quite limited and restricted to two Globular Clusters (GCs) of NGC 6822: Larsen et al. (2018) have provided abundances for NGC 6822 SC6 ([Mg/Fe]= +0.295 with rms=0.240; [Ca/Fe]= +0.228 with rms=0.170; [Ti/Fe]= +0.290 with rms=0.091) and for NGC 6822 SC7 ([Mg/Fe]= -0.180 with rms=0.208; [Ca/Fe]= +0.042 with rms=0.141; [Ti/Fe]= +0.013

with rms=0.128). They found measurements consistent with those of nearby dwarf galaxies and also the first evidence of the knee in the [α/Fe] versus [Fe/H] relation. d) NGC 6822 thanks to its modest distance has been the cross road of multi-band investigations ranging from the optical to the near-infrared (NIR) and to the mid-infrared (MIR) of Young Stellar Objects (YSO) and Asymptotic Giant Branch (AGB) stars (Letarte et al. 2002, hereinafter L02; Kinson, Oliveira & van Loon 2021; Parada et al. 2021). These investigation have been soundly complemented by low- (Kacharov, Rejkuba & Cioni 2012, hereinafter K12) and medium-resolution spectroscopy (Sibbons et al. 2012, 2015, hereinafter S12; S15). e) This galaxy has also aroused great interest concerning the search, the identification and the characterization of variable stars. Optical time series data covering a time interval of months were collected by Pietrzyński et al. (2004). They identified 116 classical Cepheids, together with sizable samples of Long Period Variables (LPVs) and eclipsing binaries (Mennickent et al. 2006). More recently, a detailed census of LPVs and candidate LPVs were also provided by collecting NIR time series: Battinelli & Demers (2011), using the wide-field imager CPAPIR at the CTIO, have found 64 LPVs; Whitelock et al. (2013), using the IRSF at SIRIUS, have provided a list of 157 LPV stars. These investigation were soundly complemented with fainter time series data collected with FORS2 at VLT by Clementini et al. (2003) and by Baldacci et al. (2005). They identified large samples of LPVs, eclipsing binaries, Chepheids and for the first time a sample of 41 candidate RR Lyrae (RRL) variables. f) NGC 6822 is one of the few nearby dwarf galaxies to host a spatially extended system of GCs. To date, have already been identified eight GCs belonging to the galaxy (Hubble 1925; Hwang et al. 2011; Huxor et al. 2013) and their structural properties are fundamental to probe the galaxy assembly process. g) NGC 6822 was one of the very first dwarf galaxies to be discovered and for this reason it held an important role in defining the scale of cosmic distances. The first distance estimate of NGC 6822 was determined by Shapley (1923) and subsequently redefined by Hubble (1925). Its stellar content was a stepping stone for the concept of stellar populations and for the cosmic distance scale. h) The mean metal-intermediate chemical composition and the identification of solid young (classical Cepheids), intermediate-age (LPVs) and old (RRLs) stellar tracers and its apparent isolation make this stellar system a very interesting laboratory for stellar pulsation and evolution and to investigate galactic evolution.

The photometric investigation available in the literature and focused on NGC 6822 have moved along two different paths. a) *Small and deep* – Detailed photometric investigations have been performed by using deep and accurate photometric images of several ACS at HST fields located across the disk of the galaxy by Cannon et al. (2012) and by Fusco et al. (2012, 2014). The color-magnitude diagrams approached the turn off of the old stellar populations and the star formation histories based on these data provided detailed information of the radial distribution of young, intermediate and old stellar populations. The same outcome applies to the ground-based optical photometry collected with 8m telescopes and to the space-based MIR photometry collected with SPITZER, because the field-of-view of the adopted detectors was quite limited and of the order of tens of arcmin squared. b) *Large and shallow* – Several optical and NIR ground-based photometric investigations have also been performed by using wide field imagers at the 2-4m class telescopes. This means that they mainly focused either on young (YSOs, massive main sequence stars) or on intermediate-age (AGB) stellar tracers over the entire body of the galaxy.

This is the first paper of a series aimed at studying the stellar content of NGC 6822 by taking advantage of optical photometry collected with wide field imagers available at the 4-8m class telescopes. In this investigation we will focus our attention on the photometric properties and the structure parameters of the galaxy, and discuss in detail the radial distribution of a broad range of stellar populations and the C/M ratio derived from the AGB stars count.

2. OBSERVATIONS AND DATA REDUCTION

Our photometric catalog was obtained by using a sizable sample of multi-band (g, r, i) images collected with Hyper-Suprime-Cam (HSC) at Maunakea Subaru Telescope. The individual images were collected by rotating the camera of 45 degrees in consecutive exposures to fill the gaps among CCDs, and to overcome difficulties with bright saturated stars (blooming) and with artifacts on individual CCDs. The HSC has a field of view (FoV) of 1.5 degrees in diameter, with a $0.17''$/pixel scale. These images include both deep and shallow exposures, acquired during three different nights: September 29th, 2014 (r-band); October 7th, 2015 and June 7th, 2016 (g and i-band). The shallow exposures include 4 r, 1 g and 3 i-band images, each with an exposure time of 30 s. The deep exposures include 14 r, 60 g and 24 i-band images, with exposure times of 300 s for the r-band and 240 s for both the g and the i-band. The HSC is

Table 2. Summary of the observing runs for NGC 6822

Run name	Dates	Telescope	Camera	N_r	N_g	N_i	multiplex
suba29	2014 Sep 29	Subaru 8.2m	Hyper Suprime-Cam	18	–	–	x 104
suba29	2015 Oct 07	Subaru 8.2m	Hyper Suprime-Cam	–	25	12	x 104
suba29	2016 Jun 07	Subaru 8.2m	Hyper Suprime-Cam	–	36	15	x 104
mp6822	2004 May 26-Jun 25	CFHT 3.6m	MegaPrime	3	3	7	x 36
dec1605	2016 May 28	CTIO 4m	DECam	4	4	4	x 34
dec1607	2016 Jul 04-05	CTIO 4m	DECam	4	4	4	x 34
int0305	2003 May 01-03	INT 2.5m	Wide Field Camera	–	6	–	x 4

NOTE—The most external HSC CCDs have not been used to obtain our photometric catalog.
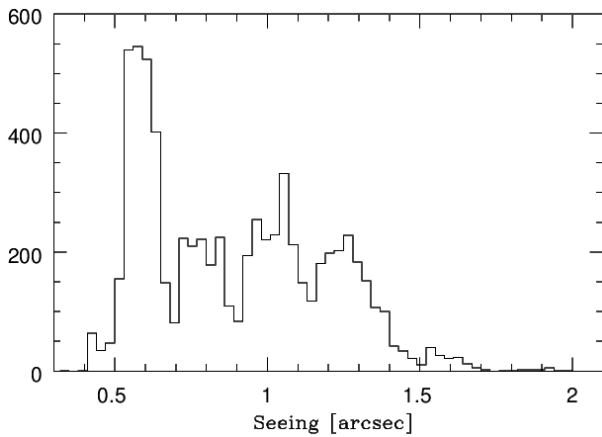
**Figure 1.** Seeing distribution of individual CCD images included in the dataset.

equipped with 104 CCDs, but the current photometric catalog does not include a few of the most external ones.

This dataset was complemented with multi-band images collected with the wide field imager MegaPrime available at the Canada-France-Hawaii Telescope (CFHT), with the Dark Energy Camera (DECam) on the Blanco telescope at Cerro Tololo Inter-American Observatory (CTIO), and with the Wide Field Camera (WFC) mounted on the Isaac Newton Telescope (INT) at La Palma. Actually, these three optical datasets were included to improve the absolute photometric calibration and the sampling of bright stars. The images from the CFHT were acquired between May 26th and June 25th, 2004 and include 3 r, 3 g and 7 i-band images and their exposure times range from 15 to 150 s. The MegaPrime has a FoV of 1x1 square degree with a $0.19''$/pixel scale. The data acquired at the Blanco telescope include 8 r, 8 g and 8 i-band images collected over three nights (May 28th, July 4th and 5th, 2016) and their exposure times range from 30 to 80 s. The

DECam has a FoV of 2.2 square degrees in diameter with a $0.27''$/pixel scale. Finally, the images from the INT include 6 g-band exposures collected during two nights on 1st and 3rd May, 2003 and have an exposure time of about 600 s. The WFC has a 34×34 arcmin FoV with a $0.33''$/pixel scale. All in all the current dataset cover 2 square degrees across the center of the galaxy and a time interval of 13 years. The seeing distribution of individual CCD images included in the dataset is plotted in Fig. 1, it suggests that 25% of the images were collected with a seeing better than $0.6''$ and 60% with a seeing better than $1''$. The log of the observing runs is summarized in Table 2. Fig. 2 shows the sky coverage of the different datasets used in this study. The left panel displays the coverage of the HSC (shallow and deep), the MegaPrime, the DECam and the WFC g, r and i-band exposures. The right panel shows the sky coverage of the infrared (IR) catalogs available in literature for NGC 6822[1]. i) Near-Infrared (NIR) catalog (black dots; S12) covering an area of 1.8 square degrees across the galaxy center and acquired at the 3.8 m United Kingdom Infrared Telescope (UKIRT) with the Wide Field CAMera (WFCAM; $0.4''$/pixel scale) as part of the UKIRT Infrared Deep Sky Survey (UKIDSS, Warren et al. 2007). ii) Mid-Infrared (MIR) photometry (red dots; Khan et al. 2015) covering the innermost (5.2×5.2 arcmin squared) central regions and collected from the mosaics of the SIRTF Nearby Galaxies Survey (SINGS; Kennicutt et al. 2003) by using the Infrared Array Camera (IRAC; $1.2''$/pixel scale) on board Spitzer Space Telescope (Spitzer). iii) MIR photometry (magenta dots) obtained with the Wide-field Infrared

---

[1] The NIR (S12) and MIR (Khan et al. 2015) catalogs are available on the VizieR database at https://vizier.u-strasbg.fr/viz-bin/VizieR
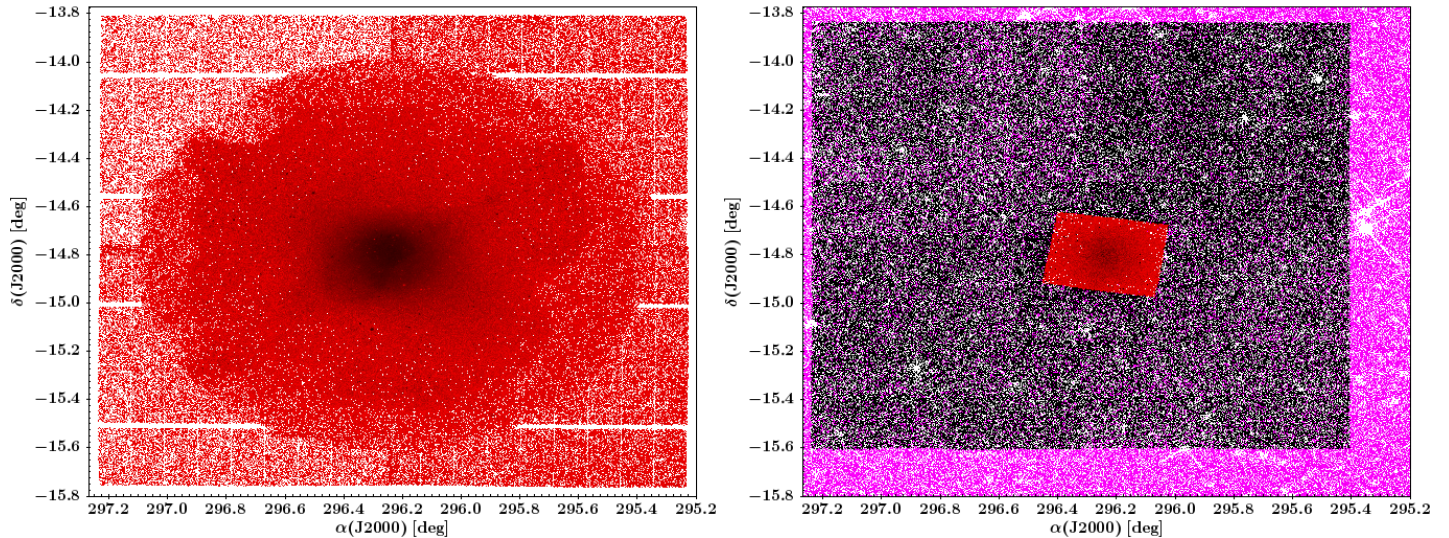
Figure 2. Left: sky coverage of the HSC (shallow and deep), MegaPrime, DECam and WFC g, r and i images. Right: same as the left panel but for the WISE (magenta dots), UKIRT (black dots) and Spitzer (red dots) datasets.

Survey Explorer (WISE; Wright et al. 2010), covering an area of 3×3 degrees centered on the galaxy. The data have been extracted from the CatWISE2020 catalog (Marocco et al. 2021) at 3.4 and 4.6 μm (W1 and W2 band, respectively), and from the AllWISE release of the WISE Source Catalog (Cutri et al. 2013) at 12 μm (W3 band). The reasons for which we decided to use the NIR and MIR catalogs will become more clear in the following sections.

The data reduction was mainly performed with the DAOPHOT-ALLSTAR-ALLFRAME packages (Stetson 1987, 1994). For the HSC images we adopted the following procedure: as a first step, the point-spread functions (PSFs) of the stars on individual images have been computed through a custom automatic pipeline, based on a suite of DAOPHOT/ALLSTAR SExtractor (Bertin & Arnouts 1996) Python Fortran routines, which discards outliers, extended sources, blends and performs the WCS alignment. Subsequently, the ALLFRAME routine was used to improve the PSF photometry on the different sets of CCDs covering the same FoV area. The instrumental magnitudes thus obtained were calibrated to the Pan-STARRS g, r, i standard system by using a list of 41,720 stars from the Pan-STARRS catalog. The derived transformation equations for each image include first- and second-order colour terms, zeropoints and linear positional terms (X and Y), and have standard deviations of 0.015, 0.012 and 0.010 mag in the g, r and i-band, respectively. The final combined and photometrically calibrated catalog contains more than 1 million objects and the limiting magnitudes range from
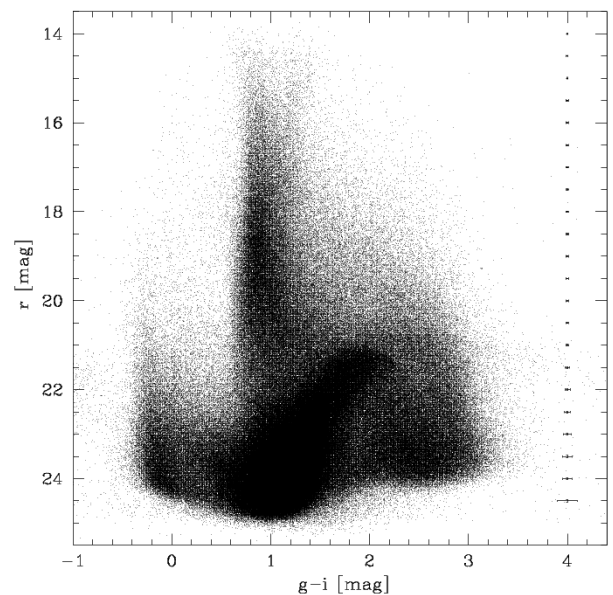
Figure 3. r, g-i CMD based on the entire optical dataset. The error bars plotted on the right side of the CMD (g-i $\sim$ 4 mag) display the intrinsic errors both in magnitude and in color (summed in quadrature).

14 to 25.8 mag in the g-band, the deepest, from 13.7 to 25.5 mag in the r-band, and from 13 to 24.9 mag in the i-band, the shallowest, thus providing the widest and most homogeneous photometric dataset ever collected for a nearby dIrr, but the Magellanic Clouds. The photometric errors typically range from 0.003 up to 0.01 mag for $g, r, i \leq 20$ mag; from 0.01 up to 0.02 mag

for $20 < g, r, i \leq 22$ mag; and increase quite steeply from 0.02 up to 0.09 for $g, r, i > 22$ mag. The r, g-i color-magnitude diagram (CMD) resulting from the entire optical dataset is plotted in Fig. 3, together with the error bars showing the intrinsic photometric errors both in magnitude and in color, for which they were summed in quadrature. The CMD shows some clear features of the NGC 6822 galaxy, such as the Young Main Sequence (YMS) at $g - i \sim -0.2 - 0$ mag and the Red Giant Branch (RGB) ranging over about 3.5 mag in magnitudes and 1.2 mag in color, but also a considerable number of foreground and background field stars, indeed the two sequences of G-type stars at $g-i \sim 1$ mag and M-type stars at $g - i \sim 2 - 3$ mag are particularly prominent.

3. IDENTIFICATION OF CANDIDATE FIELD AND GALAXY STARS

The separation between candidate field and galaxy stars is one of the fundamental issues concerning the analysis of stellar populations in nearby stellar systems. Stellar systems located at low Galactic latitudes are severely affected by field contamination, therefore, star counts and the comparison between theory and observations in both optical and near-infrared CMDs are hampered by foreground and background Galactic stars. The problem becomes even more severe for gas rich stellar systems, because they are typically affected by differential reddening. NGC 6822 is affected by the quoted limitations and to overcome these difficulties special attention was paid to the separation between field and galaxy stars.

The approach we devised differs from the approach we have already adopted for ω Cen (Calamida et al. 2020) and nearby dwarf galaxies Carina (Bono et al. 2010) and Sculptor (Martínez-Vázquez et al. 2016). NGC 6822 includes young, intermediate and old stellar tracers, therefore, we developed a new method based on 3D color-color-magnitude diagrams (CCMDs). The initial step relies on the separation between the most relevant evolutionary features of candidate field and galaxy stars. To accomplish this goal we selected two different regions located well outside the central regions of the galaxy (see yellow dots plotted in Fig. 4a). The reasons for this selection is twofold:

a) These regions are located outside the disk/bar and beyond the core radius. This means that they are less affected by crowding, therefore, their photometry is deeper and more accurate. Moreover, these regions are also less affected by differential reddening and the evolutionary sequences are intrinsically narrower.

b) Star counts of both field and galaxy stars almost balance at these radial distances. This means a proper identification of the key evolutionary features. Indeed, at larger radial distances the CMD is dominated by field stars, whereas at smaller radial distances by galaxy stars. Note that the sharp decrease in the stellar density of the most external regions is a consequence of the fact that these regions were only covered with shallow exposure times. Therefore, their limiting magnitude is 2/3 mag shallower than for the internal regions.

Fig. 4b shows the 3D CCMD, $g - r$,$r - i$,r. We performed a preliminary identification of both candidate field stars, plotted with orange/red dots, and candidate galaxy stars plotted on top with green dots. The different sequences were identified by using different view angles that help in the identification of both field and galaxy sequences. Moreover, to properly identify candidate galaxy stars we also used different sets of stellar isochrones transformed into the PanSTARRS photometric system from the BASTI database[2] covering a broad range in stellar ages and chemical compositions (see discussion in Section 5.1). To make more clear the adopted procedure, Fig. 4c shows the same stars in the CCMD, but the view is from the top of the Z-axis (r mag). Data plotted in these CCMDs allow us to properly identify candidate field stars, namely the sequence of G-type stars located at $g - r \sim 0.4$–0.8 mag and the more relevant sequence of M-type stars located at $g-r \sim 1.2$–1.5 mag (Castellani et al. 2002; Girardi et al. 2012; Robin et al. 2014). After a number of test and trial in which we took into account the luminosity and the color function we also performed a preliminary identification of galactic RGB and early AGB sequences (green dots). To further highlight the difficulties in disentangling galaxy and field sequences, Fig. 4d shows the same stars, but plotted in the $g - r$,$r - i$ color-color Diagram (CCD).

Note that candidate galaxy and field stars overlap over the entire color ranges. A glance at the data plotted in this CCD clearly shows that along the line of sight and at the quoted radial distances, field stars outnumber candidate galaxy stars. Selections only based on colors will include a significant fraction of candidate field stars among candidate galaxy stars and viceversa. As a final validation of the selection criteria adopted to identify candidate field and galaxy stars we also investigated their radial distributions. Fig. 5 show the radial distribution of the stars marked with yellow dots in

---

[2] The interested reader is referred to http://basti-iac.oa-abruzzo.inaf.it/index.html.
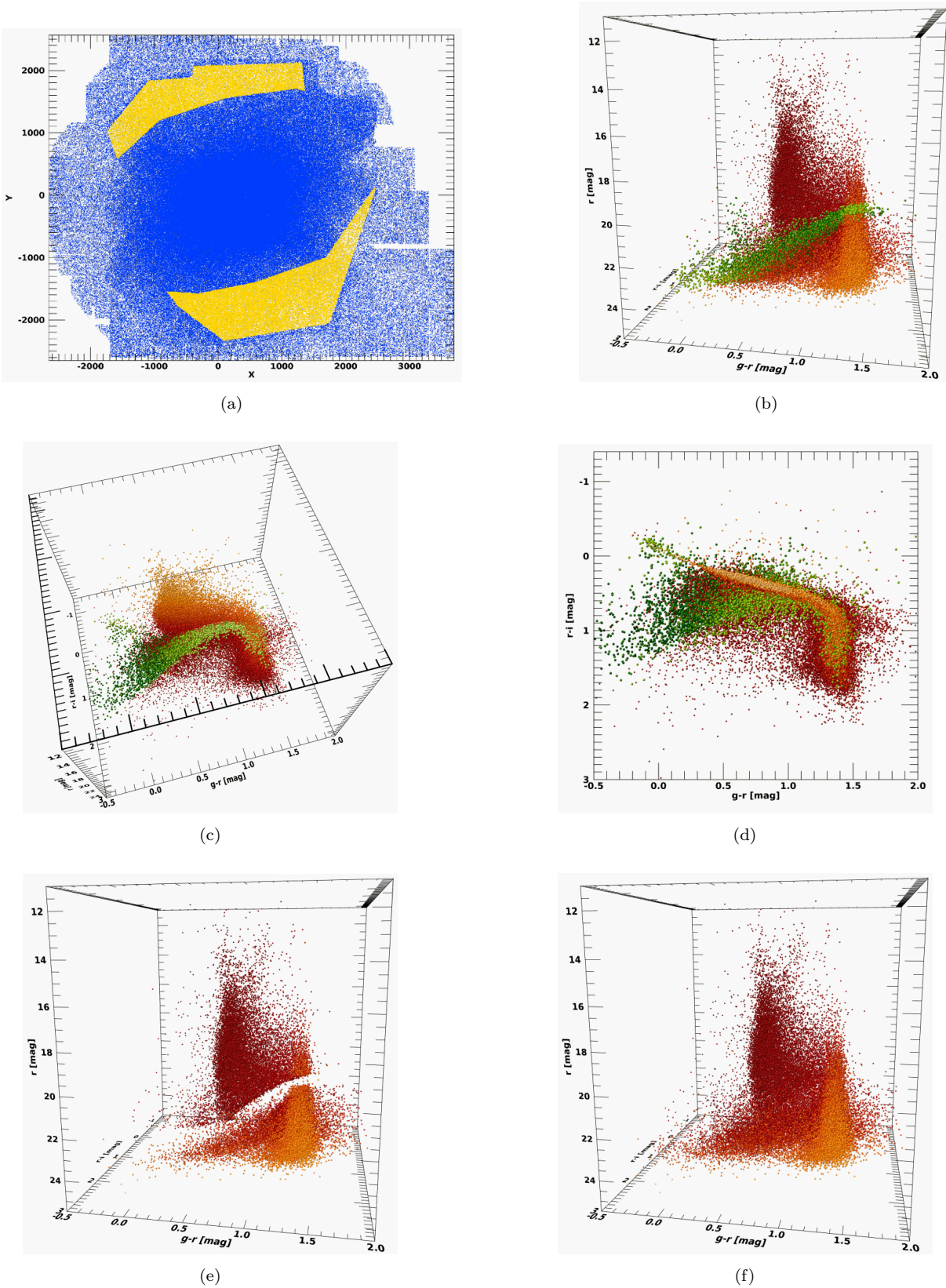
Figure 4. Panel a)– Distribution on sky of the entire optical catalog (blue dots). The yellow dots display the regions adopted for selecting candidate galaxy stars. Panel b)– g-r, r-i, r Color-Color-Magnitude diagram (CCMD). Green dots display candidate galaxy stars, while red dots candidate field stars. Panel c)– Same as Panel b), but with a different view angle. Panel d)– Same as Panel b), but the view is from the top of the z-axis, i.e. projected onto the g-r, r-i, color-color diagram (CCD). Panel e)– Same as Panel b), but we only plotted candidate field stars after the subtraction of candidate galaxy stars. Panel f)– Same as Panel e), but the gap was filled by statistically subtracting stars from the sample of candidate galaxy stars. See text for more details.
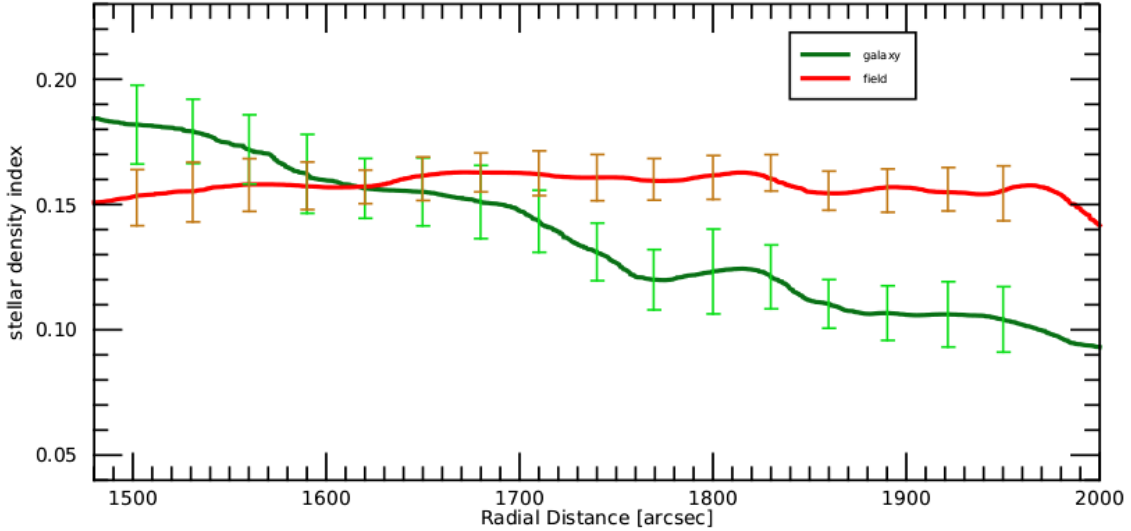
Figure 5. Surface density of candidate galaxy (green line) and field (red line) stars as a function of the radial distance for the stars marked with yellow dots in Fig. 4a. The radial distributions were smoothed by using a Gaussian kernel with unitary weight. The error bars display the standard deviation in the estimate of the surface density.

Fig. 4a. We estimated the surface density of candidate field (red line) and galaxy (green line) stars in concentric annuli of equal area and plotted them as a function of the radial distance. The radial distributions were also smoothed by assuming a Gaussian kernel with unitary weight. Data plotted in this figure show that candidate field stars have, within the errors, a flat distribution over the entire area, while the candidate galaxy stars display, as expected, a steady decrease when moving from the innermost to the outermost galaxy regions.

Subsequently, we removed the sequence of candidate galaxy stars and were left with the CCMD showed in Fig. 4e. Data plotted in this figure show that the subtraction of candidate galaxy stars caused an over subtraction of field stars in the region with colors ranging from $g - r \sim 0.0$ to $g - r \sim 1.5$ and from $r - i \sim 0.7$ mag to $r - i \sim 1.1$ mag, and with r magnitudes ranging from $r \sim 23$ to $r \sim 18.5$ mag. To overcome this problem we split the same CCMD region of the candidate galaxy stars (see green dots in Fig. 4b) in roughly two dozen of contiguous slabs. We randomly extracted in each slab of candidate galaxy stars a number of stars that allowed us to have in each slab of candidate field stars a number of stars similar (within Poisson uncertainties) to the regions of the CCMD located at the edges of the gap caused by the subtraction of candidate galaxy stars. The outcome of the random extraction of possible field stars among candidate galaxy stars is displayed in Fig. 4f, in which the gap is no more present. The new catalog of candidate field stars plotted in Fig. 4f was statistically subtracted to the entire photometric catalog (yellow plus blue dots plotted in Fig. 4a). The main outcomes of

this process were two new subsamples of candidate field and galaxy stars. The latter subsample was used to improve the selection criteria adopted to separate field and galaxy stars (yellow dots in Fig. 4a) and following once again the same steps discussed at the beginning of this section we ended up with a final catalog of candidate galaxy stars including more than 550,000 stars with at least one measurement in two different photometric bands.

The final outcome is shown in Fig. 6. The top panel displays the r, g-r CMDs for the whole photometric catalog (left), stars candidate to belong to NGC 6822 (middle) and field stars (right); the bottom panel is the same as the top panel, but for i, g-i CMDs. For the sake of clearness, we decided to plot one object over ten selected from each catalogs. Note that, when field stars were removed, some well defined evolutionary phases can be easily recognized: Young MS stars ($16 \leq i \leq 24.5$ mag, $g - i \sim 0$ mag), RSGs ($16 \leq i \leq 20.5$ mag, $1.4 \leq g - i \leq 2$ mag), the tip of the RGB ($i \sim 20.5$ mag, $g - i \sim 2$ mag), and AGB stars ($19.5 \leq i \leq 20.5$ mag, $1.8 \leq g - i \leq 3.8$ mag). The candidate field stars plotted in the right panels show that the separation between field and galaxy stars can be improved, indeed, in the region between $19.5 \leq i \leq 22.5$ mag and $1.2 \leq g - i \leq 1.8$ mag, some galaxy stars could also be present.

The catalog of the candidate galaxy stars allows us to provide accurate estimates of the absolute magnitude of NGC 6822 in all of the investigated photometric bands. The mean apparent and absolute magnitudes
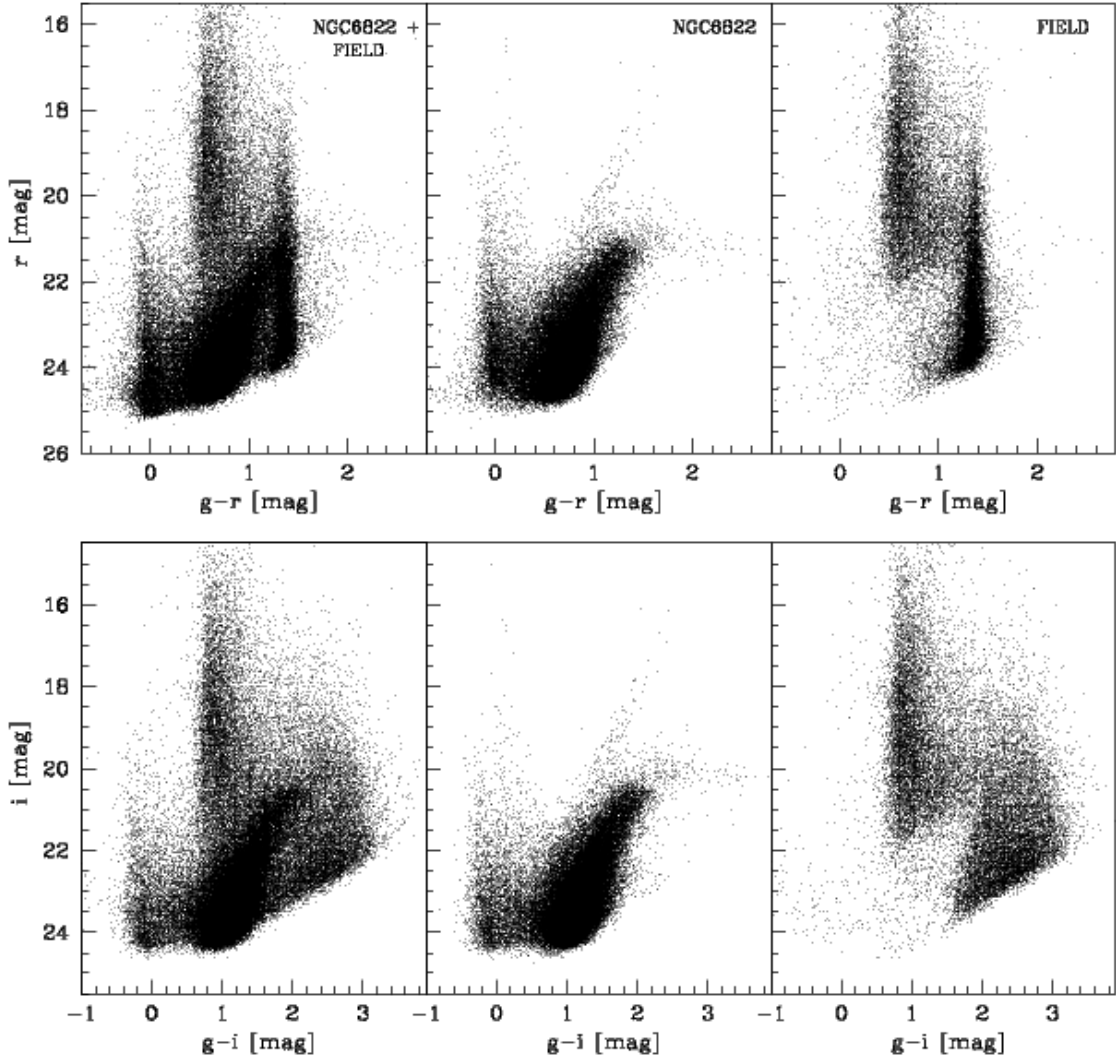
Figure 6. Left: r, g-r (upper panel) and i, g-i (lower panel) CMDs of the entire optical catalog. Middle: same as the left panels, but for candidate NGC 6822 stars. The data in this panel display several well defined evolutionary phases: Young MS stars ($16 \leq i \leq 24.5$ mag, g-$i \sim 0$ mag), RSGs ($16 \leq i \leq 20.5$ mag, $1.4 \leq g$-$i \leq 2$ mag), the tip of the RGB ($i \sim 20.5$ mag, g-$i \sim 2$ mag), and AGB stars ($19.5 \leq i \leq 20.5$ mag, $1.8 \leq g$-$i \leq 3.8$ mag). Right: same as the left panels, but for candidate field stars. The CMDs showed in this figure only display one star every ten of the global catalog.

are listed in Table 3 together with their uncertainties. We unreddened the apparent magnitudes of candidate galaxy stars by using the reddening map provided by Schlegel, Finkbeiner & Davis (1998, $E(B-V) = 0.24$ mag) and the reddening law provided by Cardelli, Clayton & Mathis (1989). Note that we decided to neglect the intrinsic reddening, since according to the reddening map by Schlegel et al. (1998) the variation across the main body of the galaxy is $\Delta E(B-V) = 0.04$ mag. This means a minimal impact on the absolute magnitudes listed in Table 3. Then the apparent unreddened magnitudes were transformed in fluxes, summed up and transformed into magnitudes once again. Subsequently, the total apparent magnitudes were transformed into

absolute magnitudes by adopting a true distance modulus of $\mu = 23.46 \pm 0.06$ mag, that is the mean value of the true distance moduli obtained by Fusco et al. (2012), by using the TRGB, and by Rich et al. (2014) by using classical Cepheids. The g, r total apparent and mean absolute magnitudes were transformed into B, V apparent and absolute magnitudes by using the following linear transformations between PanSTARRS and Johnson/Cousins photometric systems provided by Tonry et al. (2012): $g - r = 0.213 + 0.587(B - g)$ and $g - r = 0.006 + 0.474(V - r)$. More detailed transformations based on the $BVRI$ and on the g, r, i photometry available to our group will be provided in a forthcoming paper. Note that in order to estimate the

Table 3. Total apparent and absolute magnitudes for NGC 6822, the SMC and the LMC.

Band	Apparent	Absolute	Absolute[a]	Absolute for SMC[c]	Absolute for LMC[c]
	(mag)	(mag)	(mag)	(mag)	(mag)
g	8.43 ± 0.03	-15.03 ± 0.07	. . .	. . .	. . .
r	7.97 ± 0.03	-15.49 ± 0.07	. . .	. . .	. . .
i	7.68 ± 0.04	-15.78 ± 0.08	. . .	. . .	. . .
B	8.85 ± 0.05^{b}	-14.61 ± 0.08^{b}	-14.62	-16.89 ± 0.06	-18.28 ± 0.05
V	8.93 ± 0.03^{b}	-14.53 ± 0.07^{b}	-15.09	-16.29 ± 0.06	-17.60 ± 0.05
J	7.91 ± 0.10	-15.55 ± 0.12	-17.35	-17.35 ± 0.06	-18.77 ± 0.05
H	7.29 ± 0.08	-16.17 ± 0.10	-17.83	-18.05 ± 0.06	-19.52 ± 0.05
K	7.10 ± 0.10	-16.36 ± 0.12	-18.29	-18.27 ± 0.06	-19.77 ± 0.05
W1	5.86 ± 0.09	-17.60 ± 0.11	-18.08	-18.24 ± 0.06	-19.60 ± 0.05
W2	5.76 ± 0.14	-17.70 ± 0.15	-18.25	-18.26 ± 0.06	-19.59 ± 0.05
W3	4.12 ± 0.33	-19.34 ± 0.34	. . .	-20.44 ± 0.06	-21.27 ± 0.05

Note—[a] Absolute magnitudes from the literature: V and B-band magnitudes were obtained by using the total apparent magnitudes from Mateo (1998) and the same reddening and true distance modulus used for our estimates; Total NIR/MIR magnitudes were estimated by using the global unreddened flux densities from Dale et al. (2007) and the same true distance modulus used for our estimates. Note that we neglected uncertainties on individual estimates, since they are very similar to the current ones. [b] V, B total apparent and absolute magnitudes were obtained by using the linear transformations between PanSTARRS and Johnson/Cousins photometric systems from Tonry et al. (2012) (see text for more details). [c] V, B total absolute magnitudes were obtained by using the colour-colour transformations between Gaia eDR3 and Johnson/Cousins photometric systems from Riello et al. (2021) (see text for more details). J, H, K in the 2MASS system and $W1, W2, W3$ in the AllWISE system were estimated from measurements in the Gaia eDR3 catalogue.

total apparent magnitudes in $W1$ and $W2$ bands we took into account for the [3.6] and [4.5] measurements of candidate galaxy stars, covering the central regions and collected with IRAC@SPITZER, together with the $W1$ and $W2$ measurements covering the more external regions and collected by WISE. Actually, Cutri et al. (2013) found that the W1 and W2 bands photometry is consistent with the IRAC@SPITZER magnitudes in the two equivalent bands [3.6] and [4.5], respectively, with only small differences largely due to the small changes in bandpasses. This result has been confirmed in subsequent studies that found a negligible difference between the W1 and IRAC [3.6] bands, and an offset of 0.028 mag between the W2 and IRAC [4.5] bands (Papovich et al. 2016). This difference is reduced to less than 0.02 mag for late spectral-type stars. The column 4 of the same table gives the absolute magnitudes available in the literature for NGC 6822. The B, $W1$ and $W2$ magnitudes are quite similar, within the errors, to the current estimates. On the contrary, the J, H, K absolute magnitudes are, on average, two magnitudes fainter. The difference is mainly due to

the fact that the J, H, K literature estimates are based on 2MASS photometry that is shallower than UKIRT photometry and typically they did not perform a separation between candidate field and galaxy stars. The columns 5 and 6 of the table list the total absolute magnitudes for the Large Magellanic Cloud (LMC) and the Small Magellanic Cloud (SMC) in the same photometric bands used for NGC 6822, with the exception of g, r, i. Apparent magnitudes for indiviual stars in the MCs are available in the Gaia eDR3 catalogue which provides measurements in the three Gaia photometric bands G, G_{BP}, G_{RP}, in the 2MASS NIR (J, H, K) and in the AllWISE MIR ($W1, W2, W3$) bands (see Appendix B for more details). The individual apparent magnitudes were unreddened by using the reddening values provided by Joshi & Panchal (2019, $E(B-V)_{LMC} = 0.091 \pm 0.050$ mag, $E(B-V)_{SMC} = 0.038 \pm 0.053$ mag), and then the total absolute magnitudes were estimated by using the true distance moduli from Pietrzyński et al. (2019, $\mu_{LMC} = 18.477 \pm 0.004$ mag) and Graczyk et al. (2020, $\mu_{SMC} = 18.977 \pm 0.016$ mag). Finally, the G, G_{BP}, G_{RP} total absolute magnitudes were trans-

formed into B, V absolute magnitudes by using the following colour-colour transformations between Gaia eDR3 and Johnson/Cousins photometric systems from Riello et al. (2021): $G - V = -0.02704 + 0.01424(G_{BP} - G_{RP}) - 0.2156(G_{BP} - G_{RP})^2 + 0.01426(G_{BP} - G_{RP})^3$ and $G - V = -0.04749 - 0.0124(B - V) - 0.2901(B - V)^2 + 0.02008(B - V)^3$. The results show that NGC 6822 in all the listed photometric bands is fainter than the MCs. Moreover, the magnitudes in Table 3 indicate that NGC 6822 has optical-NIR colors similar to those of the MCs, and optical-MIR colors that are systematically redder than MCs with a difference of the order of one magnitude. This difference is mainly caused by the large relative number of C-rich stars identified in NGC 6822.

In this context it is worth mentioning that the total apparent magnitudes in the three WISE photometric bands can be used as diagnostics to identify active galactic nuclei (AGNs) in dwarf galaxies. Indeed, Hainline et al. (2016) used the infrared WISE color-color ($W1 - W2$, $W2 - W3$) diagnostic diagram to separate the AGNs and the so-called "composite" galaxies, defined as stellar systems having contributions to their emission-line flux from both star-formation and AGN activity (Baldwin, Phillips & Terlevich 1981; Kewley et al. 2001; Kauffmann et al. 2003). According to the current estimates, NGC 6822 has unreddened WISE colors of $W1 - W2 = 0.10$ mag and $W2 - W3 = 1.64$ mag. This means that NGC 6822 is located along the blue tail of the "composite" galaxy sequence (see Fig. 1 of Hainline et al. (2016)). This evidence taken at face value indicates that in the selected sample of composite galaxies the AGB stars, and in particular, C-rich stars can contribute to their total flux, together with young stars (YMS, RSG) and possibly with AGN activity. The current findings suggest that MIR color space should be cautiously treated in the selection of AGNs in dwarf galaxies due to the non-trivial contribution of young (Reines 2022), and in particular, of intermediate-age stellar population.

4. A NEW ESTIMATE OF THE CENTER OF THE GALAXY

The estimates of the center of NGC 6822 currently available date back to the seventies and were performed by Gallouet, Heidmann & Dampierre (1975, $\alpha_{1950} = 19^h 42^m 06^s.4$, $\delta_{1950} = -14°55'23''$), on the basis of optical photographic photometry, and from Gottesman & Weliachew (1977, $\alpha_{1950} = 19^h 42^m 04^s.2$, $\delta_{1950} = -14°56'24''$), on the basis of radio measurements of neutral hydrogen across the core of NGC 6822. In Section 5.3 we plan to investigate in detail the radial distribution of young, intermediate and old stellar tracers.

In order to provide accurate estimates of the different radial distributions we performed a new and independent estimate of the center of the galaxy. To overcome possible systematics we decided to follow two different approaches.

i) 3D histogram– To overcome possible differences among different stellar tracers, we removed from the global catalog of candidate galaxy stars the young (main sequence, red supergiants) and the intermediate-age (AGB: C-rich, O-rich; Red Clump stars) stellar tracers. We only selected RGB stars and candidate red HB stars. The motivations for these selection criteria will become more clear in Section 5.3. The left panel of Fig. 7, shows the radial distribution on sky (RA, DEC) of older stellar tracers, together with the isocontour levels. Note that the radial distribution was smoothed by assuming an unitary Gaussian kernel with sigma equal to the sum in quadrature of the errors on the position of the centroid. Finally, the Gaussians of individual candidate galactic stars were summed up and plotted on a 3D (RA, DEC, N [arbitrary units]) histogram, showed in the right panel of Fig. 7. Data plotted in this figure show that older stellar tracers attain a symmetrical spherical distribution over the entire body of the galaxy. We performed a Gaussian fit to the observed distribution and the peak of the distribution – galaxy center – is located at: R.A.(J2000) = $19^h 44^m 58^s.56$, DEC(J2000) = $-14^d 47^m 34^s.8$. The new estimate is in fair agreement with the optical and radio values, indeed it differs of 0.6 and 0.51 arcmin in RA and DEC from the estimate of Gallouet et al. (1975), and of 1.15 and 1.53 arcmin in RA and DEC from the estimate of Gottesman & Weliachew (1977).

ii) Maximum Likelihood– To provide an independent estimate of the structural parameters of NGC 6822 we adopted the publicly available code provided by Martin et al. (2008). They developed a maximum likelihood algorithm to derive the structural parameters for a number of MW satellites. They validated the algorithm on SDSS data and they found that their approach provides solid estimates even for extremely faint stellar systems. The isocontours plotted in the top panel of Fig. 8 display quite clearly that the spatial distribution of the galaxy is quite spherical and symmetrical. The coordinates of the galaxy center (see labeled values in the top panel of Fig. 8 and values listed in Table 4) are in fair agreement with the estimate based on the 3D histogram. The isocontours plotted in this panel display quite clearly the presence of candidate galaxy stars at radial distances larger than 1 degree. A similar evidence was also found by Zhang et al. (2021), but the current evidence is based on a larger sample. Moreover, the maximum likelihood solution suggests a position angle of $\theta \sim 75$ degrees, a
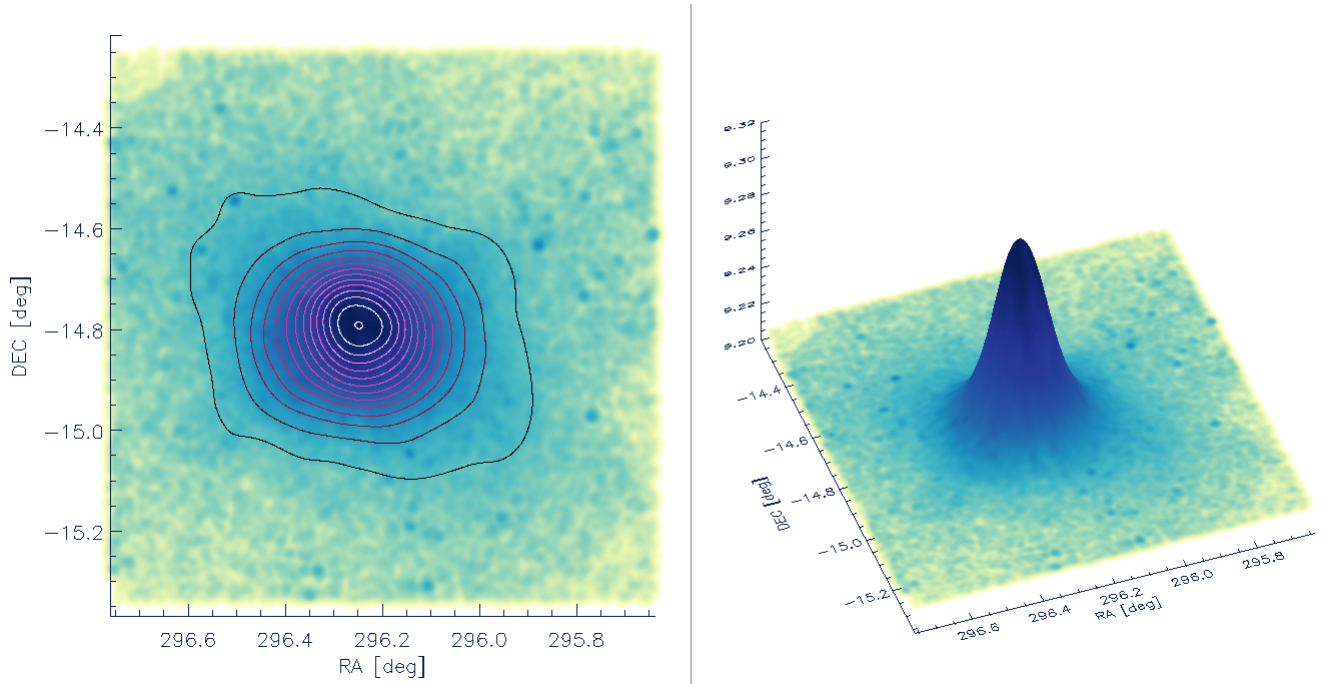
Figure 7. Left: radial distribution on sky of the old stellar tracers (RGB+RHB), smoothed by assuming a Gaussian kernel with unitary weight. Overplotted are the isocontour levels. Right: 3D histogram (RA, DEC, N in arbitrary units), showing the symmetrical spherical distribution of the old stellar tracers, obtained by summing up the Gaussian of the entire sample of candidate NGC 6822 stars.

very modest eccentricity ($\epsilon \sim 0.15$) and a R_{half}=10.2′. The current structural parameters are quite consistent with those provided by Zhang et al. (2021, orange dotted ellipse in figure) for the intermediate and old stellar tracers (RGB plus RC stars). They found a similar mean position angle ($\theta = 62$ degrees), but their mean eccentricity is a factor of three larger (0.35 vs 0.15) and their half-light radius is greater than our solution (16.13′ vs 10.20′). They also provided the variation of both the position angle and the ellipticity as a function of the major-axis radius (see their Fig. 8). They found that θ decreases from 80 to 35 degrees when moving from the innermost (r = 0.2 degrees) to the outermost (r = 0.9 degrees) galactic regions, while the eccentricity in the same regions increases from 0.2 to 0.4. These findings agree quite well with results obtained by Battinelli, Demers & Kunkel (2006) suggesting a variation in θ from 80 (r ~ 0.1 degrees) to 65 degrees (r ~ 0.6 degrees) and in ϵ from ~ 0.20 to ~ 0.38. In passing we note that the difference in eccentricity and in half-light radius, based on the maximum likelihood solution, and similar estimates in the literature is mainly due to the depth and homogeneity of the current photometric catalog across the main body of the galaxy. To constrain on a more quantitative basis the difference, we performed a new estimate of

the structural parameters by selecting two different star samples. The first sample was made considering all the stars with $20.75 < i < 23.5$ mag and $g - i > 0.5$ mag; the second sample was obtained by artificially cutting the photometric catalog to stars brighter than $i = 23.5$ mag. The results are plotted in the central and bottom panels of Fig. 8 and show that the isocontours and the structural parameters remain very similar to the global solution.

5. STELLAR POPULATIONS IN NGC 6822

The CMD of NGC 6822 has been already introduced in Sections 2 and 3. We now discuss the different stellar populations present in the galaxy and their evolutionary and structural properties. Note that in the following we focus our attention only on the catalog of candidate galaxy stars discussed in Section 3.

5.1. *Young, intermediate and old stellar tracers*

The left panel of Fig. 9 shows the i, g-i CMD of candidate NGC 6822 stars. Note that this CMD covers more than nine i-band magnitudes and shows several well-defined evolutionary phases, associated to young, intermediate and old stellar populations. On the basis of different sets of stellar isochrones covering a broad
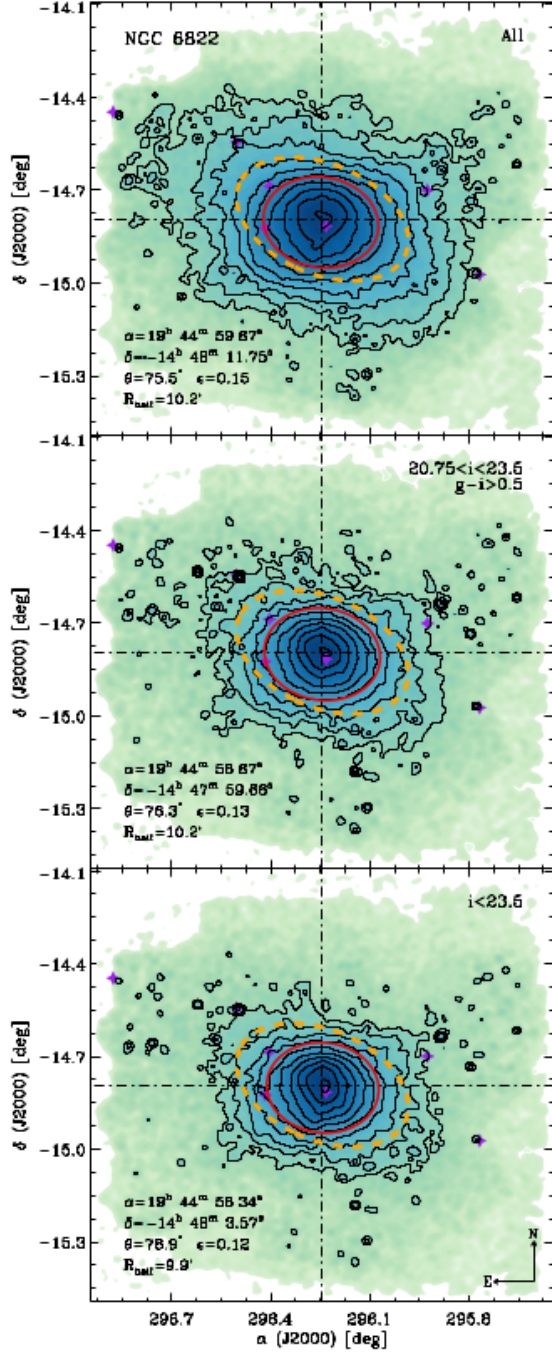
Figure 8. Top: spatial distribution of the entire sample of candidate NGC 6822 stars. The contours display the isodensity levels from 5% to 95% in a logarithmic scale. The red and orange dotted ellipses outline our fit and results from Zhang et al. (2021). The purple stars show the location of the eight known NGC 6822 GCs (e.g. Hwang et al. 2011; Huxor et al. 2013). Middle: Same as the top, but the galaxy candidates were selected both in magnitude ($20.75 < i < 23.5$ mag) and in color ($g - i > 0.5$ mag). Bottom: Same as the middle, but the sample was only selected in magnitude ($i < 23.5$ mag).

age range retrieved from the BASTI data base[3] and by visual inspection, we selected different stellar tracers, highlighted with dots of different colors (see labels). We focus our attention on the following stellar tracers.

Young stellar tracers– Young MS (violet dots) was selected considering stars with $i < 23$ mag and $-0.5 < g - i < 0.3$ mag. Note that the fainter limit in magnitude was fixed at $i = 23$ mag to avoid possible contamination of old and intermediate-age helium burning stars (HB, RC). Moreover, we also selected RSGs (blue dots) located between $16 < i < 20.5$ mag and $1.4 < g - i < 2.6$ mag. We selected these evolutionary phases because NGC 6822 is together with IC10 the prototype of star forming galaxies identified at high redshifts. Indeed, photometric and spectroscopic investigations indicate that NGC 6822 has recently experienced several star formation episodes.

Intermediate stellar tracers– Red Clump (RC; cyan dots) stars were selected in the region located at $23.7 < i < 24.3$ mag and $0.8 < g - i < 1.2$ mag. RC stars are central helium burning stars and their stellar masses are intermediate between the low-mass ($M/M_\odot \leq 1.2$) stellar structures characterized by helium cores strongly affected by electron degeneracy and the intermediate-mass ($M/M_\odot \geq 2.3$) stars that ignite quiescently central helium burning. The limits in stellar mass of the evolutionary channel producing RC stars depends on the chemical composition and their key feature is to ignite helium in a partially electron degenerate helium core. The identification of the peak associated to RC stars is based on several test and trial on 3D histograms (i, g-i, N [number of stars], r, g-i, N). Data plotted in this CMD show that RC stars overlap with RG stars. This degeneracy is caused by the so-called age-metallicity degeneracy along the RGB. Indeed, RG stars associated to stellar populations covering a broad range in age and/or in chemical composition cover, at fixed magnitude, a broad range in colors over the entire RGB. Note that in the magnitude range typical of RC stars the thickness in g-i color of the RGB is of the order of one magnitude. However, the identification of RC stars is facilitated by the empirical and theoretical evidence that the central helium burning lifetime of RC stars is systematically longer than the hydrogen-shell burning lifetime along the RGB. This means that the quoted 3D histograms display a well defined peak in magnitude and in color across the RC region (see Appendix A).

---

[3] The interested reader is referred to http://basti-iac.oa-abruzzo.inaf.it/index.html
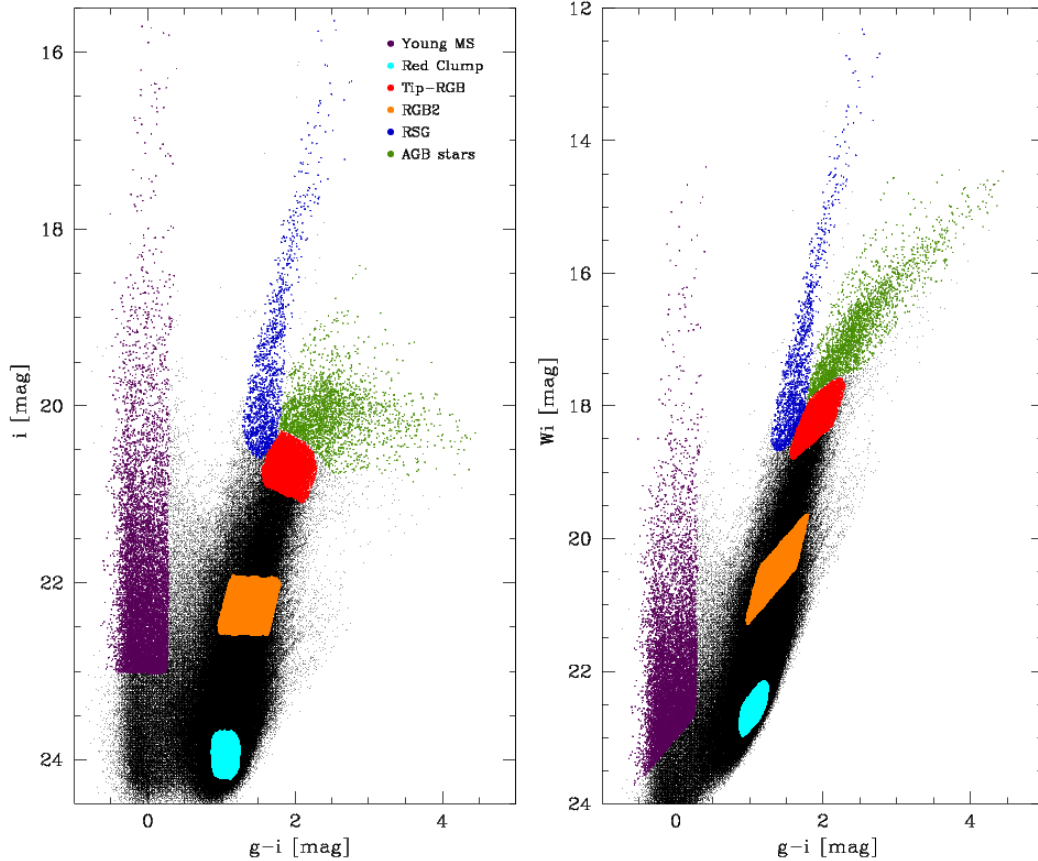
Figure 9. Left: i, g-i CMD of candidate NGC 6822 stars. Young (MS, RSG), intermediate (Red Clump, AGB) and old (TRGB, RGB2) stellar tracers are marked with dots of different colors (see labels). Right: Same as the left panel, but using the reddening-free pseudo-magnitude called Wesenheit index W_i, defined as $W_i = i - 1.32(g - i)$ mag.

In this group we also included AGB (dark green dots) stars and they were selected as the stars brighter than the Tip of the RGB (TRGB, $i \sim 20.3$ mag) and redder than the RSGs. Note that AGB stars are a mixed bag, given that all stellar populations older than ≈0.5 Gyr produce AGB stars. However, in stellar systems, like NGC 6822, that experienced recent star formation events AGB stars are typically dominated by intermediate-mass ($2 \leq M/M_\odot \leq 8$) stellar structure. In passing it is worth mentioning that the current criteria are only able to select bright AGB stars, indeed, the AGB stars fainter than the TRGB (early AGB) in optical CMD overlap with RGB stars and they can be hardly identified.

Old stellar tracers– Theory and observations indicate that TRGB stars attain a constant i-band magnitude over a broad range of stellar ages and chemical compositions. The TRGB was identified, following Sanna et al. (2008) and Bono et al. (2008), by using both the i-band luminosity function and the 3D histogram (i, g-i, N) and we found that its apparent magnitude and color are $i \sim 20.32 \pm 0.01$ mag, g-$i \sim = 1.68 \pm 0.01$ mag.

TRGB stars (red dots) were selected as the stars located between the TRGB and 0.7 mag fainter. We are aware that this region of the CMD includes RG stars associated to intermediate-age stellar populations. However their contribution, if we assume a homogeneous star formation rate over the age range producing RG stars and an initial mass function *a la Salpeter* (power law), is modest when compared with truly old (t ≥ 10 Gyr) stellar populations. Moreover, stellar populations with a chemical composition typical of NGC 6822 ([Fe/H]= -1.05, Kirby et al. 2013) stellar structures with masses larger than 2.1 $M_\odot$ are beyond the so-called red giant transition (Sweigart, Greggio & Renzini 1989, 1990). This means that they ignite quiescently central helium burning and the extension in magnitude and in color of their RG branches is quite modest when compared with truly old stellar structures. However, to take account of the change in the stellar populations that are distributed along the RGB, we also selected a fainter RGB region (RGB2, orange dots) located between the TRGB and the RC region: $22 < i < 22.5$ mag and $1 < g - i < 1.6$ mag. Note that the range in color covered by RGs in the

RGB2 sample is wider than for stars in the TRGB sample, thus further supporting degeneracy between metallicity and age.

The criteria adopted to select the different stellar tracers rely on apparent magnitudes and on colors. Therefore, they are affected by possible systematics, because NGC 6822 is affected by differential reddening. To validate the criteria adopted for selecting the different populations we plotted the same stars by using the so-called Wesenheit index (van den Bergh 1968; Madore 1976; Bono et al. 2010, 2019). The reason is twofold. i) The Wesenheit index is a pseudo-magnitude that is reddening free by construction. This means that it is independent of reddening and of differential reddening. ii) It can be derived by using measurements in two different bands. However, the Wesenheit magnitude is also affected by two main drawbacks: i) it relies on the assumption that the reddening law is universal; ii) the intrinsic error is larger than typical error affecting single band magnitudes. We defined the i-band Wesenheit magnitude by using the reddening law provided by Cardelli et al. (1989) and the central wavelengths of the Pan-STARRS photometric system (Tonry et al. 2012). In particular, we found $W_i = i - 1.32(g - i)$ mag. The right panel of Fig. 9 shows the stellar populations selected in the left panel and with the same color coding. Note that in this CMD the reddening and the differential reddening can only affect the spread in color. Data plotted in this panel show that the use of the wesenheit index, taking account for the color information, further improve the definition of several evolutionary phases. Candidate AGB stars cover more than three Wesenheit magnitudes and they are distributed along a well defined and narrow sequence. The RSG sequence is narrower than in the i, g-i CMD and fully supports the cuts in magnitude and colors adopted to separate RSG and AGB stars. The boxes adopted for selecting TRGB, RGB2 and RC stars are, as expected, slanted towards brighter magnitudes. Redder stars, at fixed magnitude, become systematically brighter in Wesenheit magnitude. As a whole they display similar features, thus suggesting that differential reddening plays a minor role in the selection of the different stellar tracers.

### 5.1.1. *Near infrared and mid infrared magnitudes*

The Wesenheit magnitude allowed us to constrain the impact that reddening and differential reddening have on the magnitude adopted for selecting the different stellar tracers. However, the g-i color is almost a factor of two more sensitive to reddening uncertainties than typical optical colors (E(B-V)/E(g-i)~0.63; Cardelli et al. 1989). To investigate on a more quantitative basis the
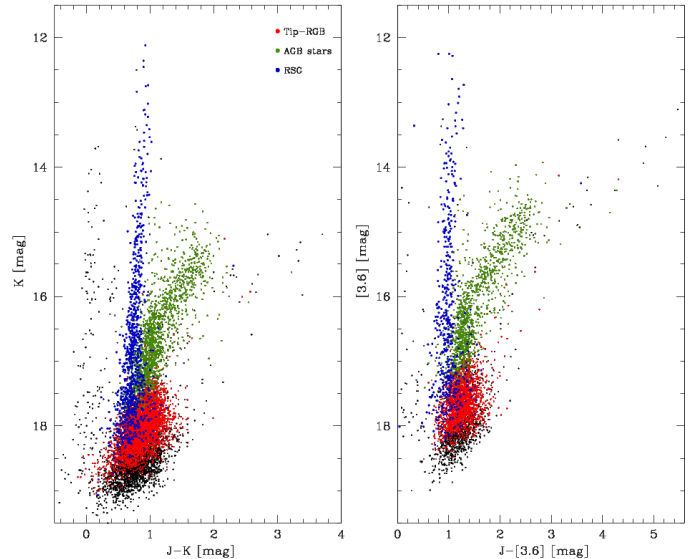
Figure 10. Left: NIR K, J-K CMD for the bright stellar populations (RSGs, AGB, TRGB) in NGC 6822. The color coding is the same as in Fig. 9. Right: Same as the left, but for the NIR-MIR *[3.6]*, *J-[3.6]* CMD.

reddening impact on the selection criteria we decided to take advantage of the NIR and MIR catalogs introduced in Section 2. The NIR dataset includes photometric measurements in J, H, K bands down to limiting magnitudes of J~20.6 mag, H~20.0 mag and K~19.6 mag (S12). The MIR photometry based on SPITZER images (Khan et al. 2015) includes measurements in the IRAC-bands and their limiting magnitudes are either similar or slightly brighter than the NIR catalog. We cross correlated the three different catalogs and we ended up with an optical-NIR-MIR catalog including ~97,500 stars with at least one optical and one NIR magnitude and with ~30,023 stars with at least one optical and one MIR magnitude.

Data plotted in the left panel of Fig. 10 show the NIR K, J-K CMD of the bright stellar populations in NGC 6822. The evolutionary sequences for RSGs and AGB are quite narrow in color and cover a wide range in magnitudes. Moreover, RSGs and AGB stars display a clear separation for K ≤ 16.5 mag. However, TRGB stars are distributed over a range of two magnitudes in K and one magnitude in J-K and overlap with RSGs and AGB stars. This means that the separation among the three different stellar tracers in this NIR CMD is prone to possible systematics. The right panel of the same figure shows the NIR-MIR *[3.6]*, *J-[3.6]* CMD for the same stellar tracers. The separation between RSGs and AGB stars becomes more clear down to *[3.6]* ∼ 17 mag, but the mix of the three different stellar tracers at fainter magnitudes is still present.
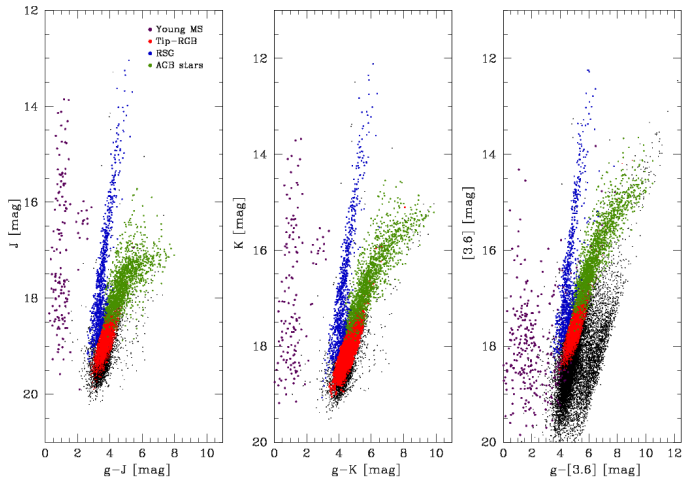
Figure 11. Same as Fig. 9, but young (MS, RSG), intermediate (AGB) and old (TRGB) stellar tracers are plotted in the two optical-NIR *J*, *g-J* (middle), and *K*, *g-K* (middle) CMDs and in the optical-MIR *[3.6]*, *g-[3.6]* CMD (right). The color coding is the same as in Fig. 9.

Data plotted in NIR and in NIR-MIR CMDs are hampered by the limited sensitivity of these colors to the effective temperature. The *g-i* color is more sensitive to the effective temperature than NIR and NIR-MIR colors, but it is significantly smaller than optical-NIR and optical-MIR colors. Indeed, the difference in color between RSG, TRGB and bright AGB stars is of the order of three magnitudes in *g-i*, but it becomes of the order of seven magnitudes in *g-K* and of eight magnitudes in *g-[3.6]*. From left to right, Fig. 11 shows the *J*, *g-J* (left) and the *K*, *g-K* (middle) optical-NIR CMDs, while the right panel shows the *[3.6]*, *g-[3.6]* optical-MIR CMD. Note that the CMDs plotted in this figure only cover bright stellar populations, indeed RC, RGB2 and a significant fraction of young MS (violet dots) stars are too faint in NIR and in MIR bands. However, brighter and cooler stellar populations (TRGB, RSG, AGB) display narrow, well defined sequences and cover a very broad range in magnitudes and in colors.

Data plotted in this figure display several interesting features worth being discussed in more detail. i) AGB and TRGB stars overlap over a substantial range in magnitude ranging from 0.3-0.4 mag in the *J*-band, to 0.5-0.6 mag in *K* and to 0.8-0.9 mag in *[3.6]*. This means that photometric selections only based on optical/NIR/MIR CMDs are, once again, prone to systematics, since TRGB and AGB stars cover similar magnitude and colors. The same outcome applies to the separation between RSGs and TRGB stars. ii) AGB stars cover more than three magnitudes in *[3.6]*, and six magnitudes in *g-[3.6]* color, thus providing a

firm validation for the separation of cool and warm AGB stars. iii) Young MS stars (violet dots) are also present, but only the very bright massive stars have been detected. The current empirical evidence indicates that the optical/NIR/MIR CMDs concerning young and intermediate-age stellar tracers bring forward several advantages (reduced sensitivity to reddening and differential reddening, strong sensitivity to effective temperature) when compared with NIR and optical CMDs, but they are affected by systematics when dealing with old stellar tracers.

5.2. *AGB: selection of C-rich and O-rich stars*

We focused our attention on AGB stars because they cover a broad range in stellar masses (M∼1–8 M$_\odot$), and in turn, stellar ages (from a few hundred Myrs to more than 10 Gyrs). This means that their spatial distributions can be safely adopted to trace back in time and in space the star formation episodes experienced by stellar systems. The AGB stars are classified according to their carbon-to-oxygen abundance ratios in three different groups: C-type (C/O>1), O-type (C/O<1, called also M-type) and S-type (C/O∼1). More recently have been suggested several subclasses and the reader interested in a more detailed discussion is referred to Boyer et al. (2011, 2015). Photometric and spectroscopic investigation indicate that C- and O-type stars typically display different radial distributions with the latter ones more centrally concentrated than the former ones. This means that a comprehensive analysis of O-rich and C-rich AGB stars covering the entire body of the galaxy will provide solid constraints on their dependence on the environment and on their metallicity distribution.

We have already mentioned in Section 5.1 that candidate AGB stars were selected in the *i*, *g-i* CMD (see Fig. 9) as the stars brighter than the TRGB (*i* ∼ 20.3 mag) and redder than the RSGs. The top panel of Fig. 12 shows in the same CMD a zoom in of the entire sample of candidate AGB stars (2788 stars, dark green dots). To further support the photometric selection of AGB stars we took advantage of the spectroscopic catalogs of C- and M-type stars available in the literature for NGC 6822. A detailed spectroscopic investigation was performed by K12. They used low-resolution spectra collected with the multi-object slit spectrograph VIMOS at VLT (ESO) and identified 150 C-type stars and 122 M-type stars. A similar spectroscopic analysis was also performed by S15 who provided a sample of 82 C-type and one anomalous M-type giant by using the AAOmega multi-fibre spectrograph at the Anglo-Australian Telescope (AAT). The spectroscopic catalogs were cross-matched with our optical catalog and
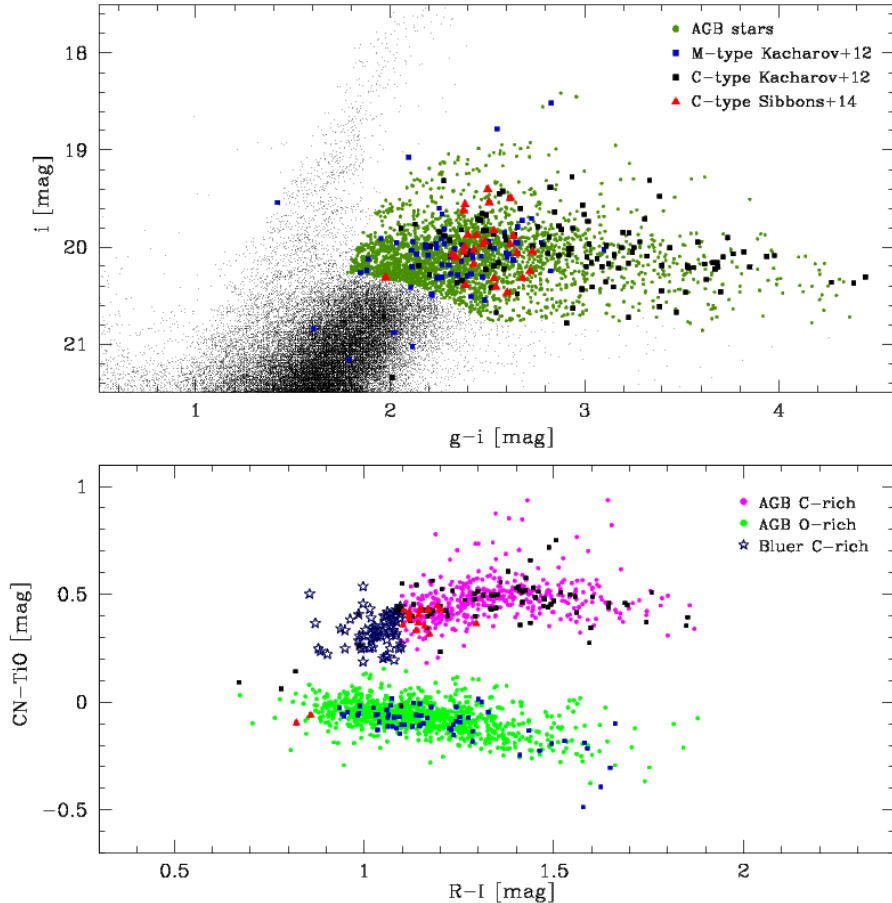
Figure 12. Top: *i*, *g-i* CMD of candidate AGB stars in NGC 6822. The CMD is zoomed on the bright portion to show the current AGB sample (dark green dots). Blue squares and red triangles display spectroscopically confirmed C-type (K12, S15), while black squares show confirmed M-type stars (K12). Bottom: *CN-TiO*, *R-I* color-color diagram for candidate AGB stars plotted in the top panel. The diagram is based on multi-band photometry collected by L02 and shows a clear separation between candidate C-rich (magenta dots) and O-rich (green dots) stars. The blue star symbols highlight the so-called bluer C-stars, as defined by L02. Symbols and colors of the spectroscopic sample (C-, M-type) are the same as the top panel.

the objects in common are plotted in the top panel of Fig. 12. The C-type identified by K12 are marked with black squares, while those identified by S15 as red triangles; the M-type identified by K12 are plotted as blue squares. A glance at the data plotted in this panel display that candidate AGB stars selected by using photometric properties agree quite well with spectroscopically selected samples. The photometric sample, as expected, outnumbers the spectroscopic sample, but they cover similar magnitude and color ranges. Note that spectroscopic M-type stars attain, as expected, colors that are systematically bluer than C-type stars. However, the two subgroups are degenerate in the *i*, *g-i* CMD because they display a clear separation neither in magnitude nor in color. In passing we also note that we investigated the few outliers located in regions typical either of the RGs or of the RSGs. We found that they have close companions and the cross-match was not univocal i.e.

there is the presence of multiple stars within the typical searching radius (1 arcsec).

Spectroscopic samples of C- and O-rich stars are based on solid diagnostics, but they are limited to the central regions of a stellar system and quite often hampered by modest statistics. To overcome these limitations we decided to use the sample of candidate C- and O-rich stars provided by L02. The key advantage of their approach is that they use a mix of broad (R, I) and narrow (CN, TiO) band photometry for the identification of candidate C- and O-rich stars. In their investigation on AGB stars in NGC 6822 they used multi-band photometry collected with both the Swope telescope and the wide field imager CFH12K at CFHT. They identified 904 candidate C-type stars, the sample was selected by using sharp cuts in the color-color plane: $(R-I)_0 > 0.90$ mag and $(CN-TiO) > 0.3$ mag. Note that to unredden the R-I color they used a mean reddening of $E(R-I)=0.20$
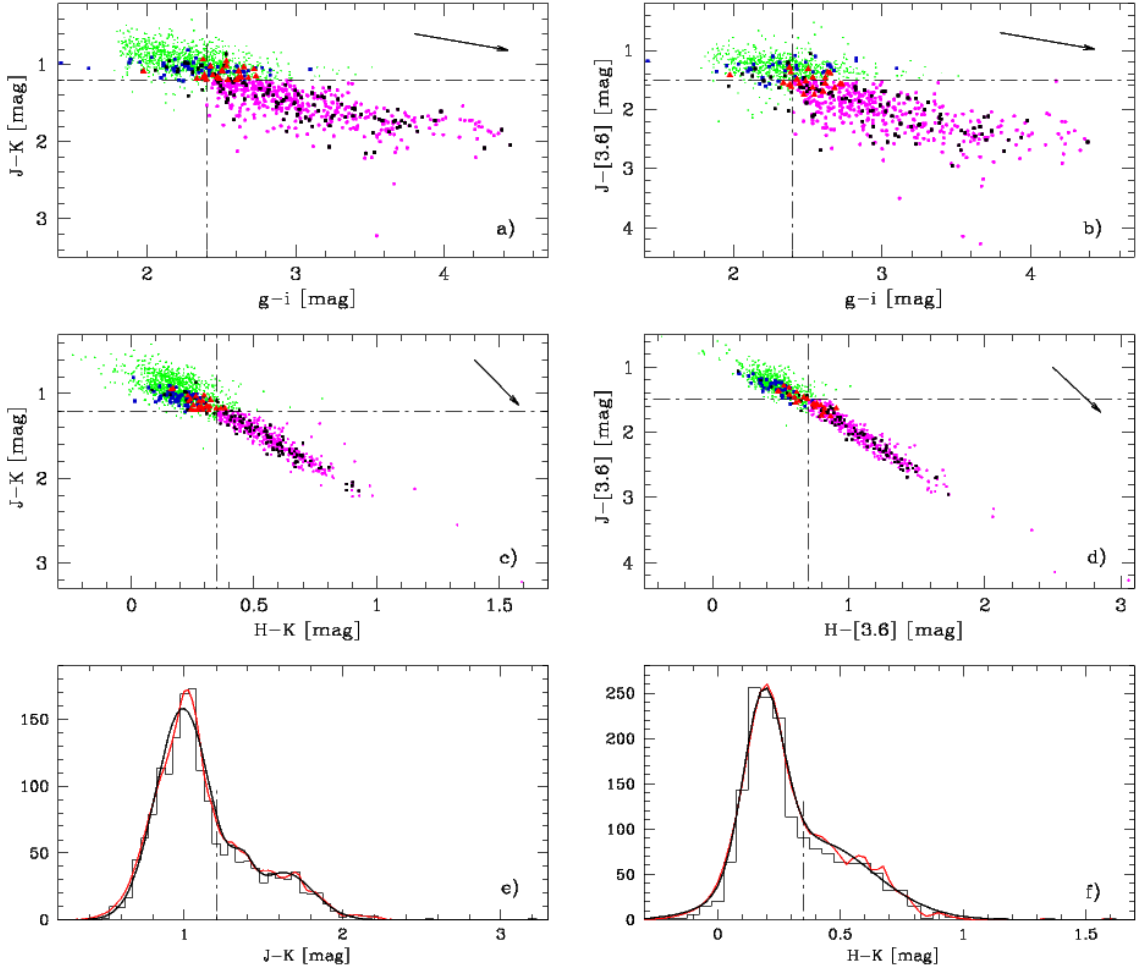
Figure 13. Panel a): Optical-NIR (J-K–g-i) CCD for candidate AGB stars plotted in the top panel of Fig. 12. The dot-dashed lines show the color cuts adopted to separate C-rich (magenta dots) and O-rich (green dots). We performed a fit of the different color distributions following the same approach adopted by Kang et al. (2006). See text for more details. Symbols and colors of the spectroscopic sample (C- and M-type) are the same as in Fig. 12. The black arrow plotted in the top right corner displays the reddening vector for an arbitrary extinction value. Panel b): Same as panel a), but for optical-NIR-MIR (J-$[3.6]$–g-i) CCD. Note that the color cuts are different. Panel c): Same as panel a), but for NIR (J-K–H-K) CCD. Panel d): Same as panel a), but for NIR-MIR (J-$[3.6]$–H-$[3.6]$) CCD. Panel e): Histogram in the NIR color J-K of candidate O- and C-rich stars. The thin red line shows the same color distribution, but smoothed with a Gaussian kernel with unitary weight and σ equal to the photometric errors (summed in quadrature) on individual color measurements. The black line shows the multi-Gaussian (three) fit of the smoothed color distribution. The dot-dashed line shows the color cut at J-$K = 1.2$ mag. Panel f): Same as the panel e), but for H-K color distribution. Note that the Gaussian fit was performed by using two Gaussians. The color limit is at H-$K = 0.35$ mag.

mag. Although this CCD is a very solid diagnostic for the identification of C-type stars, the identification of O-rich stars is hampered by the contamination of field red giants, because they attain similar colors (see Fig. 3 in L02). We have already discussed in Section 3 the approach we adopted to separate candidate field and galaxy stars and to fully exploit its potential we cross-correlated their catalog, kindly provided by the authors in electronic form, with our sample of candidate AGB stars. The results of the cross match are shown in the bottom panel of Fig. 12. Once contaminant field stars

are removed, the *CN-TiO*, *R-I* CCD becomes a very solid diagnostic to identify both C-rich (486, magenta dots) and O-rich (1002, green dots). The blue star symbols in figure highlight the so-called 'Bluer C stars', as defined by L02 ($0.8 < (R − I) < 1.1$), that we excluded from our sample of candidate C-rich because they deserve a more detailed spectroscopic analysis. Note that the number of candidate C-type stars is significantly smaller than the original sample provided by L02 due to difficulties either in the astrometric solution of the two different data sets or in separating candidate field and
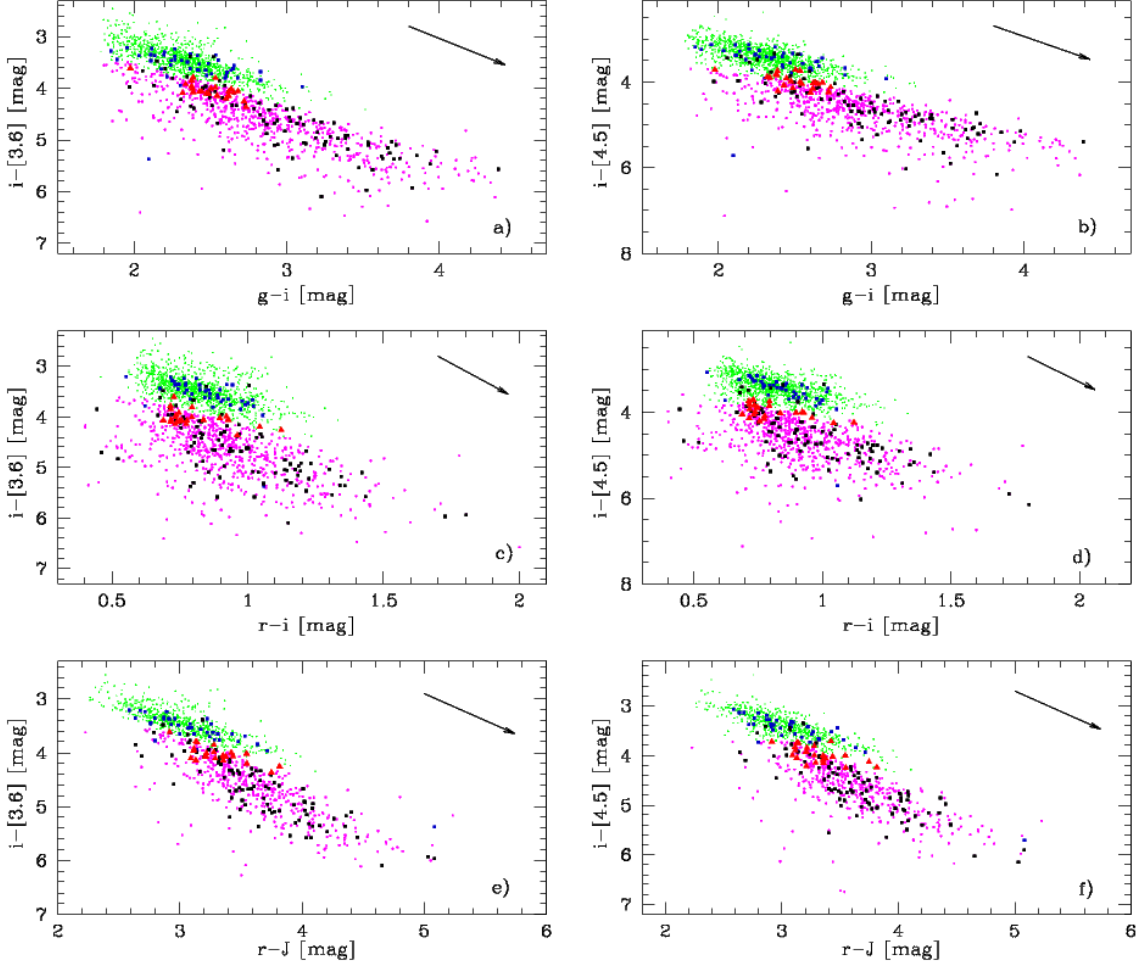
Figure 14. Panel a): Same as panel a) in Fig. 13, but for optical-MIR (i-$[3.6]$–g-i) CCD. Note that C-rich and O-rich candidates are distributed along two different, almost parallel, sequences. The C-rich candidates cover more than three magnitudes in the optical-MIR, i-$[3.6]$, color and $\sim$ 2.5 mag in the optical, g-i, color. The range in colors covered by O-rich candidates is roughly a factor of two smaller. Symbols and colors of the spectroscopic AGB sample are the same as in Fig. 12. The black arrow plotted in the top right corner displays the reddening vector for an arbitrary extinction value. Panel b): Same as panel a), but for optical-MIR (i-$[4.5]$–g-i) CCD. Panel c): Same as panel a), but for optical-MIR (i-$[3.6]$–r-i) CCD. Panel d): Same as panel a), but for optical-MIR (i-$[4.5]$–r-i) CCD. Panel e): Same as panel a), but for optical-NIR-MIR (i-$[3.6]$–r-J) CCD. The key advantage of this CCD (the same outcome applies to the CCD plotted in Panel f)) when compared with optical-MIR CCDs is that C-rich and O-rich display different slopes. Panel f): Same as panel a), but for optical-NIR-MIR (i-$[4.5]$–r-J) CCD.

galaxy stars. To further validate the current selection of AGB stars we have also plotted the spectroscopically confirmed C- and M-type stars (same as the top panel of Fig. 12). Spectroscopic data plotted in this CCD based on broad and narrow band photometry clearly show the separation between candidate C- and O-rich stars.

To further investigate this longstanding problem of the identification of C-rich and O-rich stars we decided to take advantage of the multi-band catalog we built up. In this context it is worth mentioning that Kang et al. (2006) have defined a solid photometric approach for selecting candidate C- and O-rich stars by using NIR photometry. In their investigation on NGC 6822 they

used the J-K, H-K CCD as a diagnostic to identify C- and M-type stars. They showed that the histograms in NIR colors (J-K, H-K) of candidate AGB stars have a main peak associated to M-stars and a long red tail associated to C-stars. Following this approach and the NIR color cuts (J-K=1.53 mag, H-K=0.5 mag) provided by Davidge (2005), they provided a solid separation between C- and M-type stars in NGC 6822 (see their Fig. 7). To take advantage of the current optical/NIR/MIR catalog we decided to follow a similar approach, but with different criteria to define the color cuts. Data plotted in Fig. 13 show selected AGB stars on different optical-NIR (J-K–g-i, panel a)), NIR (J-

K–H-K, panel c)) and optical-NIR/MIR (J-$[3.6]$–g-i, J-$[3.6]$–H-$[3.6]$, panels b) and d)) CCDs. For each CCD we derived histograms in color (thin grey lines in panels e) and f)) and performed a multi-Gaussian fit (black lines) of the smoothed distribution (red solid lines in panels e) and f)). The color distribution was smoothed with a Gaussian kernel with unitary weight and σ equal to the photometric errors (summed in quadrature) on individual color measurements. We performed a series of test and trials to define objective criteria for the separation of candidate C- and M-type stars, and eventually we decide to fix the color cuts as the mean between the peaks of primary and secondary Gaussian (black lines in panels e) and f)), independently of the number of Gaussians used to fit the global distribution in color. We found the following color cuts: J-K= 1.2, J-$[3.6]$= 1.5, g-i= 2.4, H-K= 0.35 and H-$[3.6]$= 0.7 and they are plotted as dashed-dotted lines in the four top panels of Fig. 13. The approach outlined in this section appears quite promising, indeed, the color sequences and the reddening vectors (black arrows) display different slopes. This suggesting that the variation in color are intrinsic and only minimally affected by differential reddening. However, this approach is still affected by thorny problems. i) The NIR, optical/NIR and optical/NIR/MIR CCDs showed in this figure display well defined color sequence when moving from M- to C-type stars. This means that they do not show any clear separation, as in the (CN-TiO), (R-I) CCD, and/or a change in the slope. This evidence is further supported by the comparison with the spectroscopic samples. Indeed, several spectroscopic C-type stars attain colors that are more typical of M-type stars and viceversa. ii) The main peak associated to M-type stars is affected by the contamination of field stars, since they typically have similar colors. This means that a solid separation between field and cluster stars is required as preliminary step to the definition of the color cuts.

To overcome these difficulties we decided to investigate other possible color combinations among the available optical, NIR and MIR magnitudes for NGC 6822 to search for CCDs that would allow us to better identify C- and M-stars. A summary of this effort is showed in Fig. 14. Data plotted in the optical/MIR CCDs (panels a,b,c,d) clearly show that C- and M-type stars are distributed along two, almost parallel sequences. The main difference between the top and the middle panels is that the spread in optical color is, at fixed optical/MIR color (i-$[3.6]$, left panels; i-$[4.5]$, right panels), significantly smaller in g-i than in r-i. Note that the separation is fully supported by the spectroscopic samples that are distributed along the expected sequences. Moreover,
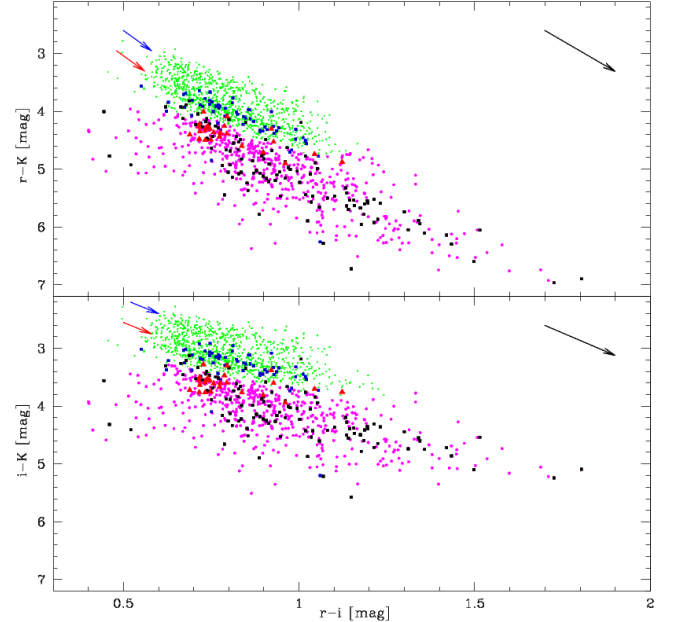

Figure 15. Top: Same as panel a) in Fig. 13, but for optical-NIR (r-K–r-i) CCD. The red arrows plotted in the top left corner display the separation in two different sequences of candidate O-rich stars. Symbols and colors of the spectroscopic AGB sample are the same as in Fig. 12. The black arrow plotted in the top right corner displays the reddening vector for an arbitrary extinction value. Bottom: Same as the top panel, but for optical-NIR (i-K–r-i). Note that in this CCD is still visible the separation of O-rich candidates into two different sequences.

the C-rich sample covers more than three magnitudes in optical-MIR colors, and from 1.5 (r-i) to 2.5 (g-i) mag in optical colors. The O-rich sample covers ranges in optical-MIR and in optical colors that are a factor of two smaller.

The same outcome applies to the optical-NIR-MIR (i-$[3.6]$–r-J and i-$[4.5]$–r-J) CCDs plotted in the bottom panels of Fig. 14; panels e), f)) CCDs. The key advantage of these CCDs is that sequences associated to O- and C-rich stars display for the first time different slopes. Indeed, the use of an optical/NIR color, together with an optical/MIR color, causes the C-rich sequence to be more slant when compared to optical colors (top, middle panels). Note that optical/NIR colors cover ranges roughly similar to the optical-MIR colors. It is worth mentioning that the C-rich and the O-rich sequences attain in the quoted CCDs slopes that differ from the slope of the reddening vectors (black arrows). This means that the dispersion in color present in all the selected CCDs is an intrinsic feature of the two stellar populations.

The mix of optical/NIR/MIR colors showed in Fig. 14 brought forward several key advantages in the identifi-
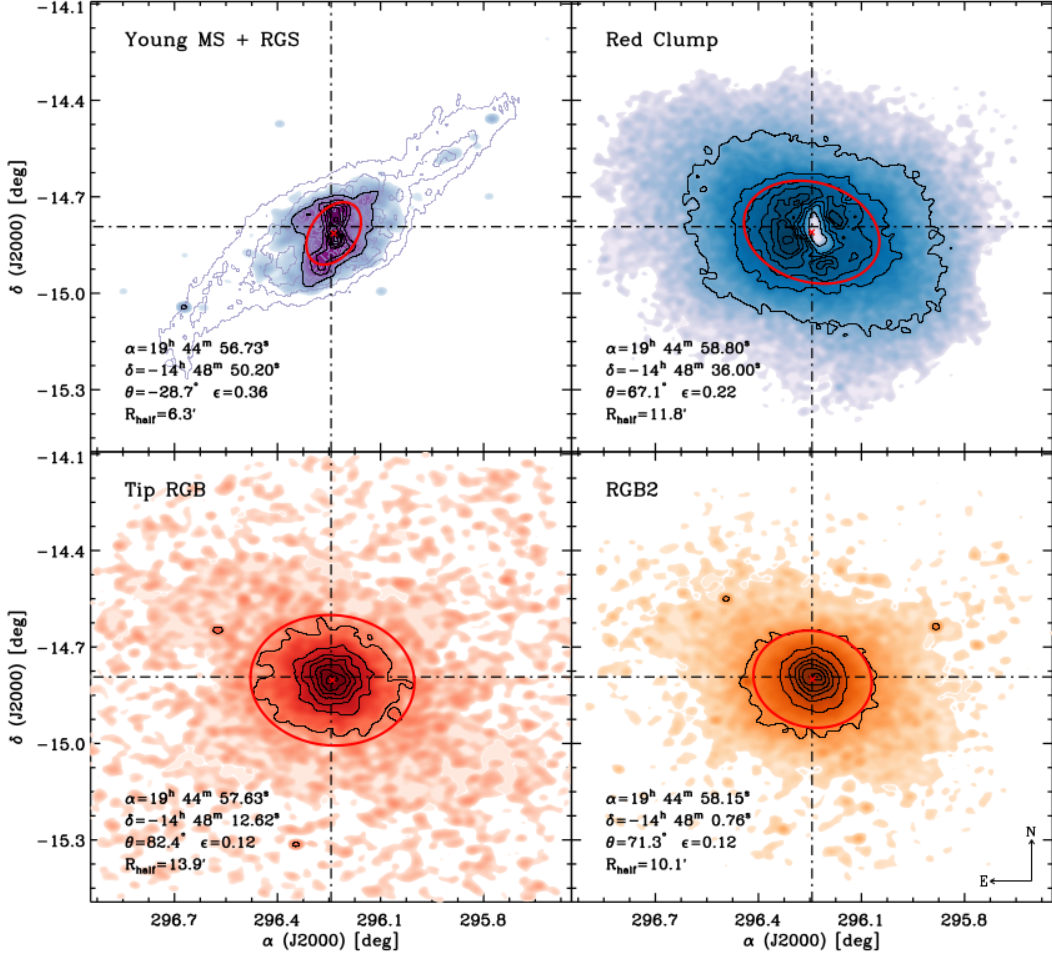
Figure 16. Spatial distributions of the young (Young MS + RSG; top-left panel), intermediate (RC; top-right panel) and old (TRGB, RGB2; bottom panels) stellar tracers in NGC 6822. The contours show the isodensity levels from 5% to 95% in a logarithmic scale. The grey contours plotted in the top-left panel (young tracers) highlight the isocontours of the HI column density map from de Blok & Walter (2000, 2003, 2006). The dot-dashed lines trace the estimated galaxy center (see Section 4). The thick red ellipses outline the fit performed according to the maximum likelihood algorithm by Martin et al. (2008). The derived structural parameters are labeled in figure and listed in Table 4.

cation of C- and M-type stars. Therefore, we decided to investigate the use of these colors to further characterize the sample of C-rich and O-rich stars. Interestingly enough we found that CCDs based on two optical-NIR colors (r-K–r-i, i-K–r-i, top and bottom panel of Fig. 15) display the same features of optical/NIR/MIR CCDs, but they also highlight a separation in two parallel sequences of candidate O-rich stars (see the blue and the red arrow plotted on the top left corner of the two panels). Note that spectroscopically confirmed O-rich stars are distributed along the two sequences, but the bluer sequence only includes a few spectroscopic identification. This empirical evidence indicates that the O-rich stars in NGC 6822 appear to include two different stellar components. Plain physics arguments suggest that the bluer sequence is younger, while the redder is

older. More quantitative constraints require a detailed comparison between theory and observations.

The current findings indicate that either optical-NIR (Fig. 15) or optical-NIR-MIR (Fig. 14) CCDs including either the r- or the i-band allow us a solid identification and characterization of C-rich and O-rich.

5.3. *Radial distributions of the different stellar tracers*

The selection of stellar tracers, covering a broad range of stellar ages, provide the opportunity to investigate on a quantitative basis their radial distributions. To provide quantitative constraints on their structural parameters we adopted the same algorithm we applied to the global catalog in Section 4. The radial distributions and the isodensity contours of the selected stellar populations are shown in Fig. 16 and in Fig. 17, the results of
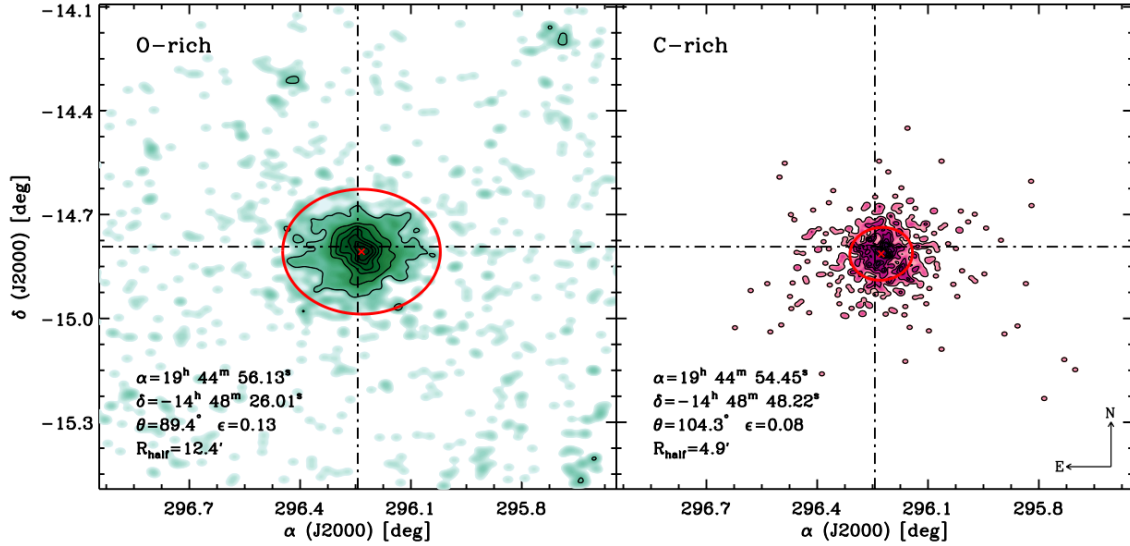
Figure 17. Same as Fig. 16, but for O- (left panel) and C-rich (right panel) stars. C-rich stars are based on the selection performed on the r-K–r-i CCD, while the O-rich stars come from our global selection of AGB stars (i, g-i CMD).

the fit are overplotted as thick red ellipses and the structural parameters are also labeled and listed in Table 4.

The top left panel of Fig. 16 shows the radial distribution on sky of young stellar tracers: MS and RSGs. A glance at the isocontours plotted in the top left panel clearly show that young stellar tracers are distributed along a well-defined bar that is mainly located between the first and the second quadrant, bending into the fourth quadrant in its southern/southern-east extension. Moreover and even more importantly, the young bar is systematically off-center (see black dashed-dotted lines and red cross) by 0.46 arcmin in RA and 1.26 arcmin in DEC. The spatial distribution of young stellar tracers is very similar to the distribution obtained by Hirschauer et al. (2020) for their RSG sample. The solution of the fit shows a moderate eccentricity, its position angle is $\theta \sim$ -29 degrees, i.e. mainly distributed along the second-fourth quadrant, and it has a modest half-light radius ($R_{half} \sim 6.3'$). The isocontours are also suggesting that the position angle is driven by young stars located outside the bar, thus suggestive of the possible presence of a disk. This working hypothesis is also supported by the isocontours of the HI column density map obtained by de Blok & Walter (2000, 2003, 2006) and overplotted on the sky distribution of young stars.

The radial distribution of intermediate-age stellar tracers (RC) when compared with young stellar tracers is significantly different (see top right panel of Fig. 16). The isocontours are far from being symmetric and in the innermost regions there is evidence of a steady decrease of RC stars along the bar made by young stars. This is an observational bias. The RC stars are relatively faint ($i \sim 24$ mag) and the innermost galactic regions are

more crowded and more affected by internal reddening. This means that our optical catalog is not complete in the innermost regions. To overcome this limitation we estimated the peak of the RC distribution by performing a Gaussian fit of the RC distribution in RA and in DEC (see red cross). Eventually, we performed the fit, at fixed center position, and the results are plotted in the same panel. The position angle is $\theta \sim 67$ degrees, i.e. mainly distributed along the first-third quadrant. Moreover, the solution of the fit indicates a smaller eccentricity ($\epsilon \sim 0.2$) and its half-light radius is almost a factor of two larger. This means that RC stars are distributed over a significant fraction of the body of the galaxy.

The bottom panels of the same figure display the radial distribution of old stellar tracers: TRGB (bottom left) and RGB2 (bottom right). We decided to investigate the radial distribution along the RGB, because plain physical arguments outlined in Section 5.1 suggest that the role of old stellar populations increases when moving from fainter (RGB2) to brighter (TRGB) RGs. The solution of the fit for TRGB stars shows an almost spherical distribution ($\epsilon \sim 0.12$) with a position angle of $\theta \sim 82$ degrees. This means that old stellar tracers in this galaxy are almost edge-on with the semi-major axis along the E-W directions and the minor axis along the N-S direction. Moreover and even more importantly, the half-light radius is larger than for young and intermediate-age stellar populations and the isocontours cover the entire area covered by our optical photometry. This means that current photometry is not approaching

Table 4. Structural parameters for the selected stellar tracers. From left to right the columns give: the stellar tracer, sky coordinates of the galaxy center, the position angle, the eccentricity, the half-light radius, difference in RA and DEC with the galaxy center estimated in Section 4 (see also Fig. 16 and 17).

Stellar tracer	α	δ	θ	ϵ	R_{half}	ΔRA	ΔDEC
	(J2000)	(J2000)	($^\circ$)		($'$)	($'$)	($'$)
Global[a]	$19^h44^m58.56^s$	$-14^h47^m34.80^s$	...	...	...	...	...
G1[b]	$19^h44^m58.56^s$	$-14^h47^m34.80^s$	75.8	0.14	10.2	...	...
G2[c]	$19^h44^m59.67^s$	$-14^h48^m11.75^s$	75.5	0.15	10.2	-0.28	0.62
G3[d]	$19^h44^m58.67^s$	$-14^h47^m59.66^s$	76.3	0.13	10.2	-0.03	0.41
G4[e]	$19^h44^m58.34^s$	$-14^h48^m3.57^s$	78.9	0.12	9.9	0.06	0.48
MS+RSG	$19^h44^m56.73^s$	$-14^h48^m50.20^s$	-28.7	0.36	6.3	0.46	1.26
RC	$19^h44^m58.80^s$	$-14^h48^m36.00^s$	67.1	0.22	11.8	-0.06	1.02
TRGB	$19^h44^m57.63^s$	$-14^h48^m12.62^s$	82.4	0.12	13.9	0.23	0.63
RGB2	$19^h44^m58.15^s$	$-14^h48^m0.76^s$	71.3	0.12	10.1	0.10	0.43
O-rich	$19^h44^m56.13^s$	$-14^h48^m26.01^s$	89.4	0.13	12.4	0.61	0.85
C-rich	$19^h44^m54.45^s$	$-14^h48^m48.22^s$	104.3	0.08	4.9	1.03	1.22

NOTE—[a] Estimate of galaxy center based on the 3D histogram of older stellar tracers (see Fig. 7). [b] Maximum likelihood performed over the entire sample of NGC 6822 candidate stars, but assuming the galaxy center based on the 3D histogram. [c] Maximum likelihood performed over the entire sample of NGC 6822 candidate stars, but keeping all the parameters free (see the top panel of Fig. 8). [d] Maximum likelihood performed by selecting candidate galaxy stars in magnitude ($20.75 < i < 23.5$ mag) and in color ($g-i > 0.5$ mag, see the middle panel of Fig. 8). [e] Maximum likelihood performed by selecting candidate galaxy stars in magnitude ($i < 23.5$ mag, see the bottom panel of Fig. 8).

the truncation radius of the galaxy. The radial distribution of the RGB2 plotted in the bottom right panel display properties that are intermediate between TRGB and RC stellar tracers. Indeed, their eccentricity is almost spherical and similar to old tracers, while the position angle is more similar to the intermediate stellar populations.

AGB stars were closely investigated and characterized, this is the reason why we decide to focus our attention on their spatial distributions (Fig. 17). Note that the C-rich stars come from the selection performed on the *r-K−r-i* CCD because they are the largest sample when compared with the selection performed on the other selected CCDs (see Section 6). The O-rich star sample used here was obtained from our global optical selection of AGB stars (*i, g-i* CMD) once C-rich stars were removed. As expected, the M-type stars (left panel) show an almost spherical distribution and their structural parameters are very similar to the structural parameters of the old stellar tracers (bottom panels of Fig. 16). The similarity applies not only to the position angle and the eccentricity, but also to half-light radius. Thus suggesting that M-type stars are dominated by old- and

intermediate-age progenitors. On the other hand, C-rich stars (right panel) are centrally concentrated and the peak of their distribution is off-center by 1.03 arcmin (RA) and 1.22 arcmin (DEC). This means that their distribution resemble the properties of the young stellar tracers ($R_{half} = 4.9'$ vs $6.3'$). However, they are spherically distributed ($\epsilon \sim 0.08$) as the old tracers, thus suggesting the key role of low mass stars for this stellar tracer. The results of the radial distributions for O- and C-rich stars are consistent with those obtained by Hirschauer et al. (2020).

6. POPULATION RATIO BETWEEN C- AND O-RICH STARS

The ratio between C- and M-type stars in a stellar population is used as a population diagnostic and to estimate the metallicity of the environment from which AGB stars formed. The reason why the C/M ratio is quite important for a quantitative analysis of resolved stellar populations is twofold. i) During the AGB phase, low and intermediate-mass stellar structures experience several physical mechanisms (3rd dredge-up, convective overshooting, mass loss, hot bottom burning) affecting

the surface chemical composition. The efficiency of these mechanisms depends on several physical parameters, and in particular, on the stellar mass and on the chemical composition. Metal-poor and metal-intermediate stellar systems are fundamental laboratories to trace the transition from M- to C-type stars. The reader interested in a more quantitative discussion is referred to Weiss & Ferguson (2009). ii) AGB stars are among the most important contributors to the integrated light of a galaxy (Renzini & Buzzoni 1986). Their role becomes even more relevant in the NIR regime where the effects of dust obscuration is significantly reduced compared to the optical bands. Moreover and even more importantly, AGB stars play a key role in the chemical enrichment of galaxies, since they produce CNO and neutron capture (s-process) elements.

We paid special care in the selection of C- and O-rich stars and the C/M ratios based on the star counts performed on a wide range of CCDs are listed in Table 5. Note that the table includes C/M ratios based on CCDs that were not discussed in Section 5.2 because they display features similar to the CCDs showed in Figs. 14 and 15. They were included to further constrain possible systematics in the use of CCDs based on different optical/NIR/MIR photometric bands. The radial distributions of candidate C- and M-type stars discussed in Section 5.3 show that the former group is significantly more centrally concentrated than the latter one. Moreover, optical, NIR and MIR datsets cover different galaxy regions (see Section 2). This means that star counts of AGB stars based on optical/NIR/MIR CCDs are sampling different regions of the galaxy. Fig. 18 shows the radial distributions of candidate C- and M-type stars selected on the r-K–r-i CCD, together with the sky area covered by MIR images collected with Spitzer (dashed black box). To provide homogeneous and accurate star counts of AGB stars we performed the selection over a box of 1000 square arcsec located across the center of the galaxy (solid black box).

The number of C- and M-type selected by using optical/NIR/MIR CCDs and the C/M ratios are listed in Table 5. The errors on the C/M ratios take account for the Poisson uncertainties. The population ratios listed in this table show that the C/M ratio remain consistent, within the errors, when moving from selections based either on NIR (J-K–H-K, C/M=0.51 ± 0.04) or on optical/NIR (J-K–g-i, C/M=0.52 ± 0.04) to a selection based on narrow and broad-band photometry
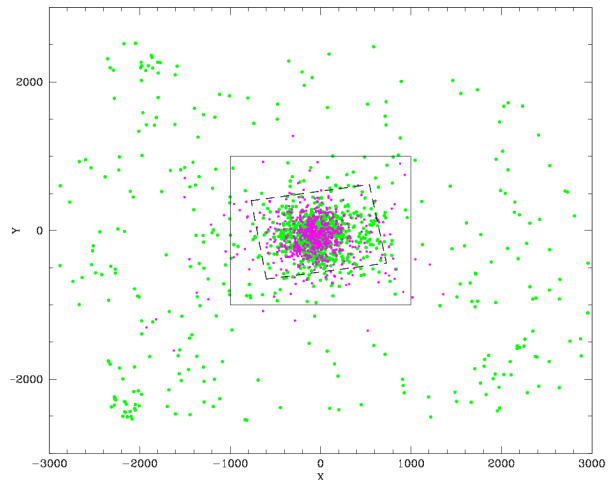
Figure 18. Radial distribution of the C- (magenta dots) and O-rich (green dots) samples selected from the r-K–r-i CCD. The black dashed rectangle delimits the field of view of the Spitzer Space Telescope; the black box of 1000 square arcsec outlines the area within which the star counts were made. Note that most of the C- and O-rich stars are located in a galaxy region entirely covered by the Spitzer dataset.

($CN - TiO$—$R - I$, C/M=0.49 ± 0.04)[4]. However, the bulk of the selections based on optical/NIR CCDs provide an average C/M ratio of 0.68 ± 0.12, while those based on optical/MIR CCDs provide on average a C/M ratio of 0.63 ± 0.04, while optical/NIR/MIR CCDs give C/M ratios of 0.70 ± 0.08. The optical and the NIR datasets adopted in this investigation cover a significant fraction of the body of the galaxy. Therefore we decided to investigate the variation of the C/M ratio when using selections based on optical/NIR CCDs. As expected the population ratios estimated over the entire body of the galaxy are on average 20% smaller than those limited to the innermost cluster regions. The difference is due to the fact that C-rich stars are centrally concentrated, while the O-rich stars cover a broader regions and their number steadily increases. This difference takes account for a significant fraction of the differences in the population ratios available in the literature (see Table 6).

We also decided to use the new population ratios to provide a preliminary estimate of the mean metallicity of AGB stars in NGC 6822. Analytical relations correlating the population ratio to the mean

---

[4] Note that in the estimate of the C/M ratio we did not include a sample of 69 fainter/bluer carbon stars, as identified by L02 (see Section 5.2). They deserve a more detailed spectroscopic analysis.

Table 5. C/M population ratios based on a variety of optical/NIR/MIR color-color diagrams and iron abundances based on empirical C/M ratio-metallicity relations.

CCD	C-rich	O-rich	C/M	[Fe/H][a]	[Fe/H][b]
C-rich and O-rich star counts over a central area of 1000 square arcsec					
CN-TiO/R-I	486	1002	0.49 ± 0.04	-1.14 ± 0.10	-1.24 ± 0.09
J-K/g-i	467	903	0.52 ± 0.04	-1.15 ± 0.10	-1.26 ± 0.09
J-[3.6]/g-i	454	743	0.61 ± 0.05	-1.19 ± 0.09	-1.29 ± 0.09
J-K/H-K	460	910	0.51 ± 0.04	-1.15 ± 0.10	-1.25 ± 0.09
J-[3.6]/H-[3.6]	461	736	0.63 ± 0.05	-1.20 ± 0.09	-1.30 ± 0.08
i-K/g-i	546	824	0.66 ± 0.05	-1.21 ± 0.09	-1.31 ± 0.08
r-K/r-i	605	764	0.80 ± 0.06	-1.26 ± 0.08	-1.34 ± 0.07
i-K/r-i	588	780	0.75 ± 0.06	-1.25 ± 0.08	-1.33 ± 0.08
i-[3.6]/g-i	755	1053	0.70 ± 0.05	-1.23 ± 0.09	-1.32 ± 0.08
i-[4.5]/g-i	662	1145	0.58 ± 0.04	-1.18 ± 0.09	-1.28 ± 0.09
r-[3.6]/r-i	701	1107	0.63 ± 0.04	-1.20 ± 0.09	-1.30 ± 0.08
i-[3.6]/r-i	714	1095	0.65 ± 0.04	-1.21 ± 0.09	-1.30 ± 0.08
r-[4.5]/r-i	680	1127	0.60 ± 0.04	-1.19 ± 0.09	-1.29 ± 0.09
i-[4.5]/r-i	686	1121	0.61 ± 0.04	-1.19 ± 0.09	-1.29 ± 0.08
i-[3.6]/r-J	520	677	0.77 ± 0.06	-1.25 ± 0.08	-1.34 ± 0.07
i-[4.5]/r-J	494	703	0.70 ± 0.06	-1.23 ± 0.09	-1.32 ± 0.08
C-rich and O-rich star counts made considering the entire area covered by our dataset					
J-K/g-i	482	1186	0.41 ± 0.03	-1.09 ± 0.11	-1.21 ± 0.10
J-K/H-K	474	1193	0.40 ± 0.03	-1.09 ± 0.11	-1.20 ± 0.10
i-K/g-i	561	1106	0.51 ± 0.04	-1.15 ± 0.10	-1.25 ± 0.09
r-K/r-i	624	1041	0.60 ± 0.04	-1.19 ± 0.09	-1.29 ± 0.09
i-K/r-i	607	1058	0.57 ± 0.04	-1.18 ± 0.09	-1.28 ± 0.09

NOTE—Iron abundances are based on the current C/M population ratios and the empirical relations provided by Battinelli & Demers (2005a)[a] and by Cioni (2009) [b].

iron abundance were provided by Battinelli & Demers (2005a) by using a sample of LG galaxies: [Fe/H]= $-1.32(\pm0.07) - 0.59(\pm0.09) \times log(C/M)$. The same relation was revised by Cioni (2009), updating metallicity values by using RGB colour method. They found: [Fe/H]= $-1.39(\pm0.06) - 0.47(\pm0.10) \times log(C/M)$.

We used these relations and the CM ratios listed in Table 5 to estimate mean metallicity for the selected AGB stars, and the new estimated iron abundances are listed in columns 5 and 6 of the same table. The errors on the iron abundances take account for the uncertainties on both the coefficients of the analytical relations and the CM ratios. The iron abundances listed in Table 5 indicate that AGB stars in NGC 6822 are independent of the adopted calibration, metal-intermediate, indeed we found a mean iron abundance of [Fe/H] ~ -1.20 ($\sigma = 0.04$

dex) and of [Fe/H] ~ -1.30 ($\sigma = 0.03$ dex), respectively. We note that the small values of the standard deviations is a consequence of the mild dependence of the adopted population ratio-metallicity relations on the C/M ratio.

Finally, we compared our results on population ratios and iron abundances with similar estimates available in the literature that are listed in Table 6. C/M ratios are quite different from each other and from our average values, with the exception of the estimate from Hirschauer et al. (2020) (0.599 ± 0.036, based on NIR/MIR CMDs) that is very similar, within the errors, to our average C/M ratio (0.63 ± 0.04) based on optical/MIR CCDs. On the other side, the mean iron abundances are in good agreement with the literature estimates, except for the value from Kang et al. (2006). Metallicity measurements for NGC 6822 were also obtained by Davidge (2003) by

Table 6. C/M ratios and iron abundances available in literature for AGB stars in NGC 6822.

C/M	[Fe/H]	Ref.[a]
1.0 ± 0.2	. . .	[1]
0.27 ± 0.03	-0.99 ± 0.02	[2]
~ 1.05	-1.3 ± 0.2	[3]
0.48 ± 0.02^{b}	-1.24 ± 0.07^{b}	[4]
0.29 ± 0.01^{c}	-1.14 ± 0.08^{c}	[4]
0.95 ± 0.04	-1.38 ± 0.06	[5]
0.599 ± 0.036	-1.286 ± 0.095	[6]

Note—[a] [1] L02; [2] Kang et al. (2006); [3] K12; [4] S12; [5] S15; [6] Hirschauer et al. (2020).
[b] C/M ratio and metallicity estimated over an area of 4 Kpc across the center of NGC 6822.
[c] C/M ratio and metallicity estimated over the entire observed area.

using the slope of the RGB ([Fe/H] = -1 ± 0.3), and from spectroscopic measurements (Venn et al. 2001: [Fe/H] = -0.49 ± 0.22; Tolstoy et al. 2001: [Fe/H] = -1 ± 0.5; Kirby et al. 2013: [Fe/H] = -1.05 ± 0.01). Our estimates agree quite well with spectroscopic measurements of old stellar populations.

7. SUMMARY AND FINAL REMARKS

We performed a detailed optical photometric analysis of the nearby dIrr galaxy NGC 6822. We carried out PSF photometry of a large set of g (61), r (18) and i-band (27) images collected with the wide field imager HSC available at the Subaru Telescope. The individual images have a FoV of 1.5 degrees in diameter and they include 104 CCDs. The dataset includes both shallow ($t \sim 30$ s) and deep ($t \sim 240$–300 s) exposures collected in very good seeing conditions ($\leq 0.9''$ for 50% of the images). These images were complemented with a 13 g, r, i images collected with the wide field imager MegaPrime available at CFHT, with two dozen g, r, i images collected with DECAM available at CTIO 4m Blanco telescope and with 6 g-band images acquired with the WFC available at INT. These data cover the same sky area covered by the SUBARU dataset, and they have exposure times ranging from 15 to 600 s and seeing similar to the HSC images. The individual images cover a FoV of 1x1 square degree (MegaPrime), of 2.2 degrees in diameter (DECAM) and of 34×34 arcmin (WFC), and they were included to improve the absolute photometric calibration and the sampling of bright stars. All in all the current photometric dataset covers an area of 2 square degrees across the galaxy center with three different photometric bands. We performed PSF photometry over 7115 individual CCD images by using the suits of codes DAOPHOT-ALLSTAR-ALLFRAME. The final catalog includes more than 1 million stars with at least one measurement in two different photometric bands. The maximum number of measurements per star range from 74 (g), to 28 (r) and to 42 (i). In total, in the three photometric bands we performed 4×10^{7} photometric measurements of objects across the entire field of view. The current catalog is the widest and most homogeneous photometric dataset ever collected for a nearby dIrr, but the Magellanic Clouds. The limiting magnitudes range from 14 to 25.8 mag (σ=0.04 mag) in the g-band, the deepest, from 13.7 to 25.5 mag (σ=0.05 mag) in the r-band, and from 13 to 24.9 mag (σ=0.09 mag) in the i-band, the shallowest.

To provide a detailed analysis of stellar populations across the entire FoV of the current dataset, we developed a new approach to identify candidate field and galaxy stars. We took advantage of the three different photometric bands and the new algorithm is an iterative procedure based on the 3D CCM diagram. We identified a training set of candidate galaxy stars located at a few arcmin from the galaxy center and the key evolutionary sequences were subtracted from the global 3D CCM diagram. After two iterations, we ended up with a catalog of candidate galaxy stars including more than 550,000 stars with at least one measurement in two different photometric bands.

Finally, the global optical photometric catalog was cross correlated with the NIR (S12) and MIR (Khan et al. 2015; Marocco et al. 2021) catalogs available in the literature. The NIR catalog includes JHK photometry and it is based on the UKIRT images covering almost the same sky area of our optical dataset, while the MIR catalogs include both the IRAC photometry from images collected with SPITZER and covering the innermost regions of the galaxy, and the CatWISE and AllWISE photometry obtained from the WISE survey and covering an area of 3×3 degrees across the center of galaxy. The global optical-NIR-MIR catalog includes more than 65,000 stars with at least two measurements in optical, in NIR and in MIR photometric bands.

The global optical-NIR-MIR catalog has been the stepping stone for several interesting results concerning the stellar content of NGC 6822.

(i) We estimated apparent and absolute total magnitudes in the nine photometric bands adopted in the current investigations. The absolute magnitude range from $\sim$ -15 to -16 mag in the three optical (g, r, i) bands,

from $\sim$ -15.5 to -16.5 mag in the three NIR (J, H, K) bands, and from $\sim$ -17.6 to -19.3 mag in the three MIR ($W1, W2, W3$) bands. We also compared the current estimates with the absolute magnitudes of the MCs, that were estimated from the Gaia eDR3 catalogue, suggesting that NGC 6822 is fainter in the optical regime than the MCs. However, optical-MIR colors suggest that NGC 6822 is systematically redder than MCs. The difference is mainly caused by the high number of C-rich stars identified in the former system. Furthermore, we found that NGC 6822 in the MIR color-color diagram ($W1-W2, W2-W3$; Hainline et al. 2016) is located in the blue tail of the so-called "composite" stellar systems (Baldwin et al. 1981; Kewley et al. 2001; Kauffmann et al. 2003), i.e. dwarf galaxies in which the emission-line flux includes contributions from both AGN and star formation activity. Thus suggesting that this diagnostic is also prone to possible systematics introduced by AGB stars.

(ii) We performed a new and independent estimate of the center of galaxy by using two different approaches: 3D histogram and maximum likelihood. The 3D histogram method was applied to the old stellar tracers, and we found that the coordinates of the galaxy center are: R.A.(J2000) = $19^h 44^m 58^s.56$, DEC(J2000) = $-14^d 47^m 34^s.8$. We also used the maximum likelihood algorithm from Martin et al. (2008) to estimate structural parameters and the coordinates of the galaxy center agree, within the errors, with the 3D histogram. The difference with previous estimates available in the literature is of the order of 1.15 arcmin in RA and 1.53 arcim in DEC. The spatial distribution and the isocontours of the whole catalog show that the galaxy is almost spherically and symmetrically distributed and includes stars at radial distances larger than 1 degree. This evidence indicates that the truncation radius of this galaxy is well beyond the current estimates. Moreover, the solution of the fit provided a position angle of $\theta \sim 75$ degrees and a very modest eccentricity ($\epsilon \sim 0.15$) that are in quite fair agreement with similar estimates available in literature (Battinelli et al. 2006, Zhang et al. 2021).

(iii) The reduction strategy we devised provided deep and accurate CMDs. The i, g-i CMD of candidate galaxy stars (Fig. 9) covers more than nine i-band magnitudes. This CMD shows several well-defined evolutionary sequences (Young MS, RSG, RGB, RC, AGB) suggesting the presence of young, intermediate-age and old stellar populations in the galaxy. We selected the different stellar tracers on the optical CMD and in order to overcome possible systematics due to the differential reddening affecting this galaxy, we validated our selections by using the Wesenheit index and by taking

advantage of both NIR and MIR photometry. Special attention was paid to the identification of AGB stars. We adopted the the same approaches suggested in literature (L02, Kang et al. 2006) and investigated new optical-NIR-MIR color combinations to further improve the identification and characterization of C- and O-rich stars. We found that the *CN-TiO*, *R-I* CCD (defined by L02) and a series of new optical-NIR, optical-MIR and optical-NIR-MIR CCDs are very solid diagnostics to identify both C-rich and O-rich stars. The former one was already known in the literature, but the region covered by M-type stars is affected by field star contamination. The latter ones are very promising because C- and O-rich stars are distributed along either two almost parallel sequences or along two sequences with different slopes. In passing we also note that the optical-NIR r-K−r-i and i-K−r-i CCDs display a separation in two parallel sequences of candidate O-rich stars, suggesting that they might include a younger (bluer sequence) and an older (redder sequence) AGB component. We compared the slopes of the sequences defined by candidate C- and O-rich in the different CCDs with the slopes of the respective reddening vectors, finding that they all differ from each other. This means that the dispersion in color present in the adopted CCDs is an intrinsic feature of AGB stars and it is minimally affected by differential reddening. Moreover, the current identifications of C- and O-rich samples are fully supported by the position of the spectroscopically confirmed C- and M-type stars provided by K12 and by S15.

(iv) We investigated the radial distributions and provided the structural parameters for the different stellar tracers selected in the optical CMD. The results show that young stellar tracers (MS+RSG) are distributed along a well-defined bar that is off-center by 0.46 arcmin in RA and 1.26 arcmin in DEC; they have a modest half-light radius ($R_{half} \sim 6.3'$) and the young stars located outside the bar suggest the possible presence of a disk ($\theta \sim$ -29 degrees). Indeed, their isocontours seems to follow very well the isocontours traced by the HI column density map (de Blok & Walter 2000, 2003, 2006). The intermediate-age stellar tracers (RC) display isodensity contours that are far from being symmetric, they are distributed over a significant fraction of the body of the galaxy ($R_{half} = 11.8'$) and have a smaller eccentricity when compared with young stellar tracers ($\epsilon \sim 0.2$ vs 0.4). The structural properties of the two selected old stellar tracers, TRGB and RGB2 stars, differ from each other. The TRGB stars show an almost spherical distribution ($\epsilon \sim 0.1$), are almost edge-on with the semi-major axis along the E-W directions and the minor axis along the N-S direction ($\theta \sim 82$ degrees) and have the

largest half-light radius among the other stellar populations ($R_{half} \sim 14'$). On the other hand, the RGB2 stars display properties that are similar to both TRGB and RC stellar tracers ($\epsilon \sim 0.1$, $\theta \sim 71$ degrees and $R_{half} \sim 10'$). Moreover, we also found that O- and C-rich stars (AGB) have different properties. The O-rich stars have structural parameters very similar to that of the old tracers ($\epsilon \sim 0.1$, $\theta \sim 89$ degrees and $R_{half} = 12.4'$), thus indicating that they are dominated by old- and intermediate-age progenitors. On the contrary, the C-rich stars are more centrally concentrated and have structural parameters similar to both young, indeed the peak of the distribution is off-center and $R_{half} = 4.9'$, and old stellar tracer ($\epsilon \sim 0.1$).

(v) We estimated the C/M population ratios based on the star counts performed on the selected CCDs, obtaining on average a C/M ratio of 0.68 ± 0.12 for optical/NIR CCDs, a C/M of 0.63 ± 0.04 for optical/MIR CCDs, a C/M of 0.70 ± 0.08 for optical/NIR/MIR CCDs and a C/M of 0.49 ± 0.04 for the narrow and broad-band photometry (*CN-TiO–R-I*) CCD. We also provided an estimate of the mean metallicity of AGB stars by using the current C/M population ratios and the empirical relations provided by Battinelli & Demers (2005a) and by Cioni (2009). We found mean iron abundances of [Fe/H] $\sim$ -1.20 ($\sigma = 0.04$ dex) and of [Fe/H] $\sim$ -1.30 ($\sigma = 0.03$ dex), respectively. Mean metallicity values are in fair agreement with the literature estimates (e.g., K12, S12, Hirschauer et al. 2020, Davidge 2003, Tolstoy et al. 2001) suggesting a metal-intermediate iron abundance.

The approach developed in the current investigation and the definition of new photometric diagnostics to investigate evolutionary properties of stellar populations in nearby stellar systems are a good viaticum for future optical-NIR-MIR photometric surveys. In this context the incoming optical survey by the Vera Rubin Observatory is going to play a key role, since the main survey plans to cover the entire southern sky every three nights in six different photometric bands (u, g, r, i, z, y) with limiting magnitudes ($\sim$27-28 mag) that will allow us a complete census of stellar populations older than 10 Gyrs (Main Sequence turn-off) over the entire Local Group.

APPENDIX

### A. IDENTIFICATION OF THE PEAK ASSOCIATED TO RC STARS

We already mentioned in section 5.1 that RC stars are solid tracers of intermediate-age stellar tracers. However, the identification of the peak associated to RC stars is far from being trivial, in a stellar system like NGC 6822, because the magnitudes and colors of RC stars in optical CMDs overlap with RGB stars. To overcome this limitation we adopted the same approach suggested by Sanna et al. (2008) for investigating stellar populations in IC10. Fig. 19 shows the 3D histogram of a i, $g - i$ CMD. The CMD was split with a grid in magnitude and color and the Z-axis shows the number of stars per grid point. The number of stars was smoothed with a Gaussian kernel with an unitary weight and σ equal to the Poisson error associated to the star count. We performed a series of test and trials to properly identify the optimal bin size in magnitude and in color and Fig. 19 shows the final outcome. Data plotted in this figure display, from left to right, several well defined, but relatively shallow, evolutionary sequences, namely the young MS, the RSG and the AGB stars. The steady increase in star counts located in the central region of the CMD is associated, from top to bottom, to TRGB and RGB stars. A preliminary comparison with evolutionary models suggests that the main peak located at $i \sim 24$ mag and $g - i \sim 1$ mag is caused by RC stars. A more detailed discussion concerning the comparison between theory and observations will be addressed in a forthcoming paper (Tantalo et al. 2022, in preparation).

To constrain on a more quantitative basis the location of RC stars we isolated the star counts associated to RG stars and estimated the ridge line in magnitude. Fig. 20 shows the ridge line in magnitude (green line) and its first and second derivatives (red and cyan lines). The maximum in the ridge line and the minimum in the first derivative located at $i \sim 23.9$–24.0 mag trace the RC stars.

B. SELECTION OF CANDIDATE GALAXY STARS FOR THE MAGELLANIC CLOUDS

The selections for the Magellanic Clouds were obtained by querying the *Gaia* eDR3 database. In particular, we selected a sky area with a $20°$ radius around the centre of the LMC and with a sky area with $11°$ radius for the SMC by using the following selection criteria to control the quality of the data: not `duplicated_source`; with color `bp_rp` measured; with astrometric solutions either with 5- or 6-parameters; not QSO; `ruwe`< 1.4; $G < 20.5$; $C^* < 1.0$. The
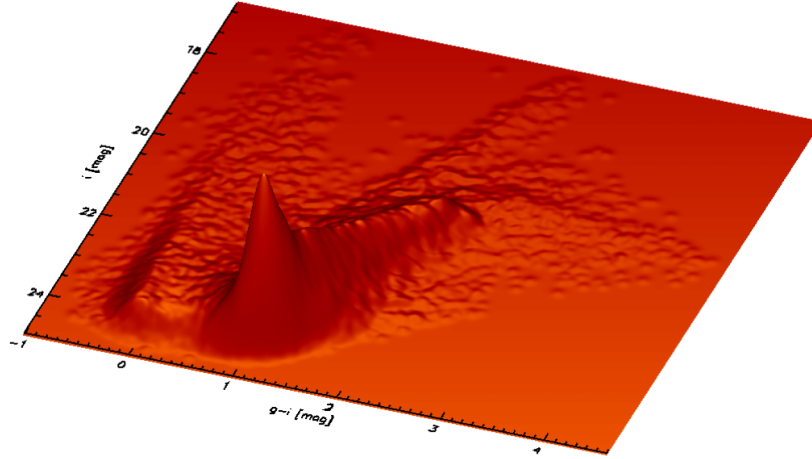
Figure 19. 3D histogram of the i, $g - i$ CMD. The view is from the faint to the brighter limit of the CMD. Note that in this CMD we are plotting all the stars with at least one measurement in g and i bands. The Z-axis is in arbitrary units. From bluer to redder colors the relatively shallow sequences are associated to young MS, to RSG and to AGB stars. The steady increase in the star counts present in the central regions is associated to RG stars. The main peak is associated to RC stars.
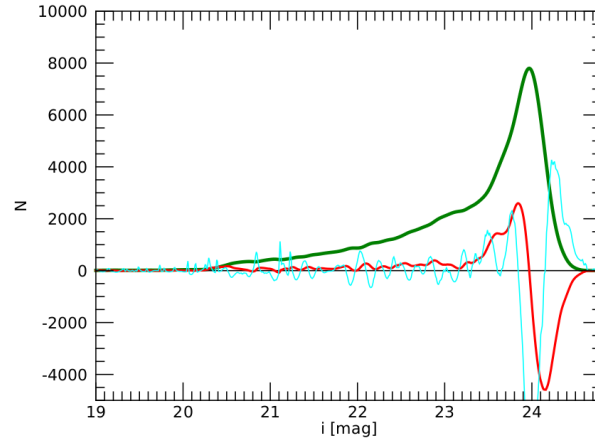
Figure 20. Ridge line in magnitude (i-band, green line) of the star counts associated to RG stars showed in Fig. 19. The red and cyan lines show, respectively, the first and the second derivative of the ridge line.

C^* is the corrected `phot_bp_rp_excess_factor` introduced by Riello et al. (2021) wich helps to remove background galaxies; bright QSOs can be identified by using the `agn_cross_id` table included in the *Gaia* release.

We ended up with a sample including 4,134,870 objects for the SMC and 14,716,026 for the LMC (see the top-left panels of Fig. 21 and 22). The exquisite quality of *Gaia* astrometric data allowed us to separate the stellar populations of the MCs from the foreground field stars by using the proper motion selection criteria. To determine the mean proper motion of both LMC and SMC we used sub-samples of objects that are closer than 0.5° to the centres of the galaxies and then we computed a Gaussian fit of the individual μ_{α^*} and μ_δ distributions. Therefore, we obtained the centres of proper motion at [0.68, -1.23] mas yr^{-1} for the SMC and [1.89,0.36] mas yr^{-1} for the LMC. Subsequently, we selected all the objects compatibles, within 10 times the errors, with the quoted mean proper motions (see the top-right panel of Fig. 21 and 22). Finally, we minimised the foreground contamination by selecting stars with `parallax`/`parallax`$_{error}$<5. This parallax cut excludes solutions that are not compatible with being distant enough to be part of the LMC or SMC, and therefore possible foreground contamination from Milky Way stars. The final samples include 2,380,151 stars for the SMC and 12,456,270 for the LMC (see the middle panels of Fig. 21 and 22). We also took advantage of the pre-computed cross-matches of the *Gaia* catalog with visual and infrared large surveys (Marrese et al. 2019), in particular, with 2MASS (see the bottom panels of Fig. 21 and 22) to further constrain the properties of candidate galaxy stars.
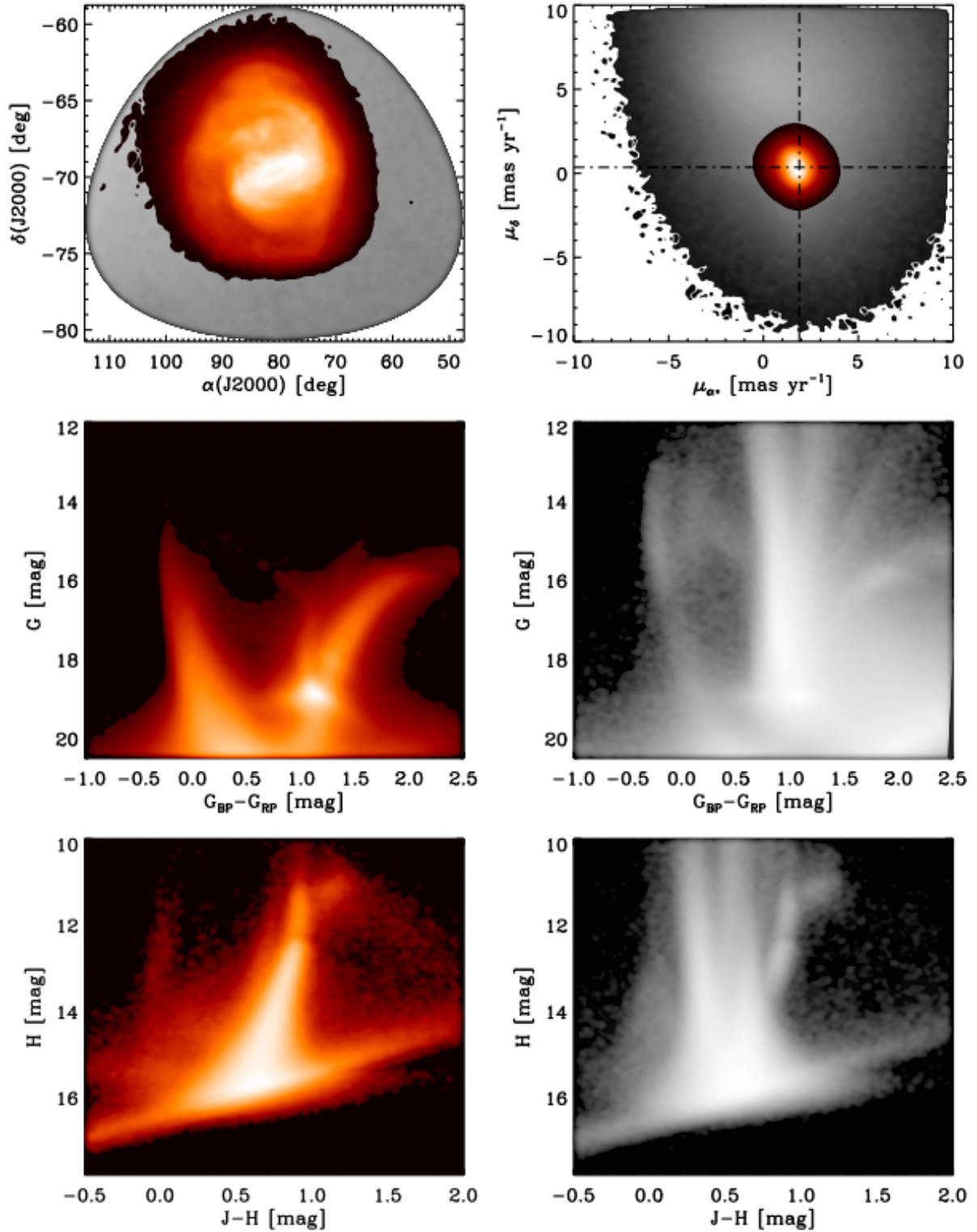
Figure 21. Top: sky coverage (left) and proper motions (right) of the candidate LMC stars (coloured). The grey region highlights candidate field stars. Middle: Optical, $G, G_{BP} - G_{RP}$, CMD for candidate LMC (left) and field (right) stars. Bottom: Same as the middle, but for the NIR, $H, J - H$, CMD.
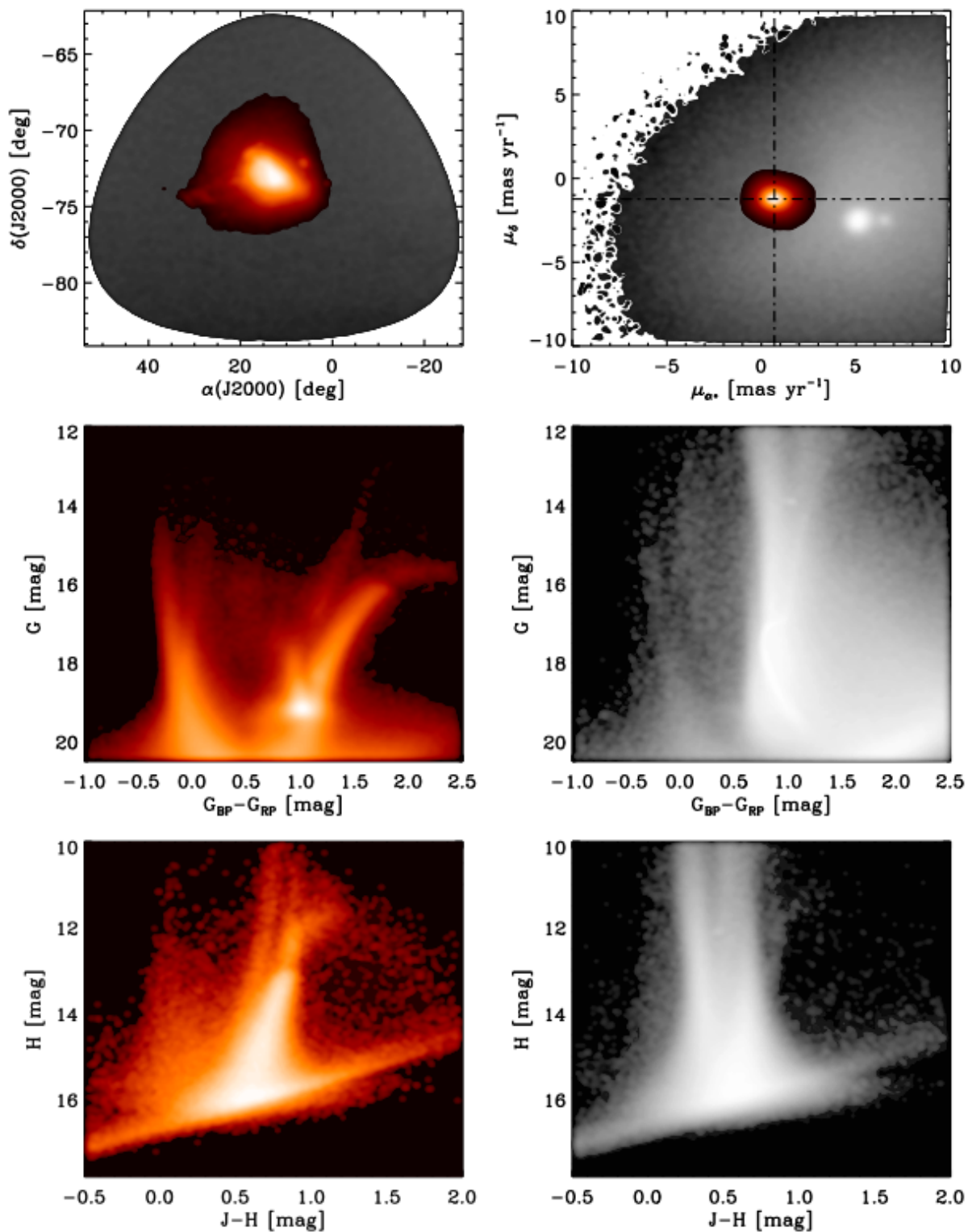
Figure 22. Same as the Fig. 21, but for candidate SMC and field stars.

REFERENCES

Astropy Collaboration, Robitaille, T. P., Tollerud, E. J., et al. 2013, A&A, 558, A33. doi:10.1051/0004-6361/201322068

Baldacci, L., Rizzi, L., Clementini, G., Held, E. V. 2005, A&A, 431, 1189. doi:10.1051/0004-6361:20041684

Baldwin, J. A., Phillips, M. M., & Terlevich, R. 1981, PASP, 93, 5. doi:10.1086/130766

Battinelli, P. & Demers, S. 2005a, A&A, 434, 657. doi:10.1051/0004-6361:20042278

Battinelli, P. & Demers, S. 2011, A&A, 525, A69. doi:10.1051/0004-6361/201015470

Battinelli, P., Demers, S., & Kunkel, W. E. 2006, A&A, 451, 99. doi:10.1051/0004-6361:20054718

Bertin, E. & Arnouts, S. 1996, A&AS, 117, 393. doi:10.1051/aas:1996164

Boyer, M. L., McDonald, I., Srinivasan, S., et al. 2015, ApJ, 810, 116. doi:10.1088/0004-637X/810/2/116

Boyer, M. L., Srinivasan, S., van Loon, J. T., et al. 2011, AJ, 142, 103. doi:10.1088/0004-6256/142/4/103

Bono, G., Iannicola, G., Braga, V. F., et al. 2019, ApJ, 870, 115. doi:10.3847/1538-4357/aaf23f

Bono, G., Stetson, P. B., Sanna, N., et al. 2008, ApJL, 686, L87. doi:10.1086/593013

Bono, G., Stetson, P. B., VandenBerg, D. A., et al. 2010, ApJL, 708, L74. doi:10.1088/2041-8205/708/2/L74

Bono, G., Stetson, P. B., Walker, A. R., et al. 2010, PASP, 122, 651. doi:10.1086/653590

Calamida, A., Zocchi, A., Bono, G., et al. 2020, ApJ, 891, 167. doi:10.3847/1538-4357/ab77c0

Cannon, J. M., O'Leary, E. M., Weisz, D. R., et al. 2012, ApJ, 747, 122. doi:10.1088/0004-637X/747/2/122

Cannon, J. M., Walter, F., Armus, L., et al. 2006, ApJ, 652, 1170. doi:10.1086/508341

Cardelli, J. A., Clayton, G. C., & Mathis, J. S. 1989, ApJ, 345, 245. doi:10.1086/167900

Castellani, V., Cignoni, M., Degl'Innocenti, S., et al. 2002, MNRAS, 334, 69. doi:10.1046/j.1365-8711.2002.05461.x

Cioni, M.-R. L. 2009, A&A, 506, 1137. doi:10.1051/0004-6361/200912138

Clementini, G., Held, E. V., Baldacci, L., Rizzi, L. 2003, ApJL, 588, L85. doi:10.1086/375633

Cutri, R. M., Wright, E. L., Conrow, T., et al. 2013, Explanatory Supplement to the AllWISE Data Release Products, by R. M. Cutri et al.

Dale, D. A., Gil de Paz, A., Gordon, K. D., et al. 2007, ApJ, 655, 863. doi:10.1086/510362

Davidge, T. J. 2003, PASP, 115, 635. doi:10.1086/375389

Davidge, T. J. 2005, AJ, 130, 2087. doi:10.1086/491706

de Blok, W. J. G. & Walter, F. 2000, ApJL, 537, L95. doi:10.1086/312777

de Blok, W. J. G. & Walter, F. 2003, MNRAS, 341, L39. doi:10.1046/j.1365-8711.2003.06669.x

de Blok, W. J. G. & Walter, F. 2006, AJ, 131, 343. doi:10.1086/497829

Du, X., Shapley, A. E., Tang, M., et al. 2020, ApJ, 890, 65. doi:10.3847/1538-4357/ab67b8

Feast, M. W., Whitelock, P. A., Menzies, J. W., Matsunaga, N. 2012, MNRAS, 421, 2998. doi:10.1111/j.1365-2966.2012.20525.x

Fusco, F., Buonanno, R., Bono, G., et al. 2012, A&A, 548, A129. doi:10.1051/0004-6361/201220554

Fusco, F., Buonanno, R., Hidalgo, S. L., et al. 2014, A&A, 572, A26. doi:10.1051/0004-6361/201323075

Gallart, C., Aparicio, A., & Vilchez, J. M. 1996, AJ, 112, 1928. doi:10.1086/118153

Gallouet, L., Heidmann, N., & Dampierre, F. 1975, A&AS, 19, 1

Gieren, W., Pietrzyński, G., Nalewajko, K., et al. 2006, ApJ, 647, 1056. doi:10.1086/505574

Girardi, L., Barbieri, M., Groenewegen, M. A. T., et al. 2012, Red Giants as Probes of the Structure and Evolution of the Milky Way, 26, 165. doi:10.1007/978-3-642-18418-5_17

Gottesman, S. T. & Weliachew, L. 1977, A&A, 61, 523

Graczyk, D., Pietrzyński, G., Thompson, I. B., et al. 2020, ApJ, 904, 13. doi:10.3847/1538-4357/abbb2b

Hainline, K. N., Reines, A. E., Greene, J. E., et al. 2016, ApJ, 832, 119. doi:10.3847/0004-637X/832/2/119

Harris, C. R., Millman, K. J., van der Walt, S. J., et al. 2020, Nature, 585, 357. doi:10.1038/s41586-020-2649-2

Hirschauer, A. S., Gray, L., Meixner, M., et al. 2020, ApJ, 892, 91. doi:10.3847/1538-4357/ab7b60

Hodge, P., Smith, T., Eskridge, P., et al. 1991, ApJ, 379, 621. doi:10.1086/170534

Hubble, E. P. 1925, ApJ, 62, 409. doi:10.1086/142943

Huxor, A. P., Ferguson, A. M. N., Veljanoski, J., et al. 2013, MNRAS, 429, 1039. doi:10.1093/mnras/sts387

Hwang, N., Lee, M. G., Lee, J. C., et al. 2011, ApJ, 738, 58. doi:10.1088/0004-637X/738/1/58

Joshi, Y. C. & Panchal, A. 2019, A&A, 628, A51. doi:10.1051/0004-6361/201834574

Kacharov, N., Rejkuba, M., & Cioni, M.-R. L. 2012, A&A, 537, A108. doi:10.1051/0004-6361/201117383

Kang, A., Sohn, Y.-J., Kim, H.-I., et al. 2006, A&A, 454, 717. doi:10.1051/0004-6361:20054763

Kauffmann, G., Heckman, T. M., Tremonti, C., et al. 2003, MNRAS, 346, 1055. doi:10.1111/j.1365-2966.2003.07154.x

Kennicutt, R. C., Armus, L., Bendo, G., et al. 2003, PASP, 115, 928. doi:10.1086/376941

Kewley, L. J., Dopita, M. A., Sutherland, R. S., et al. 2001, ApJ, 556, 121. doi:10.1086/321545

Khan, R., Stanek, K. Z., Kochanek, C. S., Sonneborn, G. 2015, ApJS, 219, 42. doi:10.1088/0067-0049/219/2/42

Kinson, D. A., Oliveira, J. M., & van Loon, J. T. 2021, MNRAS, 507, 5106. doi:10.1093/mnras/stab2386

Kirby, E. N., Cohen, J. G., Guhathakurta, P., et al. 2013, ApJ, 779, 102. doi:10.1088/0004-637X/779/2/102

Larsen, S. S., Brodie, J. P., Wasserman, A., Strader, J. 2018, A&A, 613, A56. doi:10.1051/0004-6361/201731909

Lee, M. G., Freedman, W. L., & Madore, B. F. 1993, ApJ, 417, 553. doi:10.1086/173334

Lee, H., Skillman, E. D., & Venn, K. A. 2006, ApJ, 642, 813. doi:10.1086/500568

Letarte, B., Demers, S., Battinelli, P., Kunkel, W. E. 2002, AJ, 123, 832. doi:10.1086/338319

Madore, B. E. 1976, MNRAS, 177, 157. doi:10.1093/mnras/177.1.157

Madore, B. F., Rigby, J., Freedman, W. L., et al. 2009, ApJ, 693, 936. doi:10.1088/0004-637X/693/1/936

Marocco, F., Eisenhardt, P. R. M., Fowler, J. W., et al. 2021, ApJS, 253, 8. doi:10.3847/1538-4365/abd805

Marrese, P. M., Marinoni, S., Fabrizio, M., et al. 2019, A&A, 621, A144. doi:10.1051/0004-6361/201834142

Martin, N. F., de Jong, J. T. A., & Rix, H.-W. 2008, ApJ, 684, 1075. doi:10.1086/590336

Martínez-Vázquez, C. E., Stetson, P. B., Monelli, M., et al. 2016, MNRAS, 462, 4349. doi:10.1093/mnras/stw1895

Massey, P., Armandroff, T. E., Pyke, R., et al. 1995, AJ, 110, 2715. doi:10.1086/117725

Mateo, M. L. 1998, ARA&A, 36, 435. doi:10.1146/annurev.astro.36.1.435

McConnachie, A. W. 2012, AJ, 144, 4. doi:10.1088/0004-6256/144/1/4

Mennickent, R. E., Gieren, W., Soszyński, I., Pietrzyński, G. 2006, A&A, 450, 873. doi:10.1051/0004-6361:20054359

Neugent, K. & Massey, P. 2019, Galaxies, 7, 74. doi:10.3390/galaxies7030074

Papovich, C., Shipley, H. V., Mehrtens, N., et al. 2016, ApJS, 224, 28. doi:10.3847/0067-0049/224/2/28

Parada, J., Heyl, J., Richer, H., et al. 2021, MNRAS, 501, 933. doi:10.1093/mnras/staa3750

Patrick, L. R., Evans, C. J., Davies, B., et al. 2015, ApJ, 803, 14. doi:10.1088/0004-637X/803/1/14

Pietrzyński, G., Gieren, W., Udalski, A., et al. 2004, AJ, 128, 2815. doi:10.1086/425531

Pietrzyński, G., Graczyk, D., Gallenne, A., et al. 2019, Nature, 567, 200. doi:10.1038/s41586-019-0999-4

Reines, A. E. 2022, Nature Astronomy, 6, 26. doi:10.1038/s41550-021-01556-0

Renzini, A. & Buzzoni, A. 1986, Spectral Evolution of Galaxies, 122, 195. doi:10.1007/978-94-009-4598-2_19

Rich, J. A., Persson, S. E., Freedman, W. L., et al. 2014, ApJ, 794, 107. doi:10.1088/0004-637X/794/2/107

Riello, M., De Angeli, F., Evans, D. W., et al. 2021, A&A, 649, A3. doi:10.1051/0004-6361/202039587

Robin, A. C., Reylé, C., Amôres, E. B., et al. 2014, EAS Publications Series, 67-68, 199. doi:10.1051/eas/1567036

Sanna, N., Bono, G., Stetson, P. B., et al. 2008, ApJL, 688, L69. doi:10.1086/595551

Schlegel, D. J., Finkbeiner, D. P., & Davis, M. 1998, ApJ, 500, 525. doi:10.1086/305772

Shapley, H. 1923, Harvard College Observatory Bulletin, 796, 1

Sibbons, L. F., Ryan, S. G., Cioni, M.-R. L., et al. 2012, A&A, 540, A135. doi:10.1051/0004-6361/201118365

Sibbons, L. F., Ryan, S. G., Napiwotzki, R., Thompson, G. P. 2015, A&A, 574, A102. doi:10.1051/0004-6361/201423981

Stetson, P. B. 1987, PASP, 99, 191. doi:10.1086/131977

Stetson, P. B. 1994, PASP, 106, 250. doi:10.1086/133378

Stott, J. P., Sobral, D., Smail, I., et al. 2013, MNRAS, 430, 1158. doi:10.1093/mnras/sts684

Sweigart, A. V., Greggio, L., & Renzini, A. 1989, ApJS, 69, 911. doi:10.1086/191331

Sweigart, A. V., Greggio, L., & Renzini, A. 1990, ApJ, 364, 527. doi:10.1086/169434

Taylor, M. B. 2005, Astronomical Data Analysis Software and Systems XIV, 347, 29

Tolstoy, E., Irwin, M. J., Cole, A. A., et al. 2001, MNRAS, 327, 918. doi:10.1046/j.1365-8711.2001.04785.x

Tonry, J. L., Stubbs, C. W., Lykke, K. R., et al. 2012, ApJ, 750, 99. doi:10.1088/0004-637X/750/2/99

van den Bergh, S. 1968, JRASC, 62, 145

Venn, K. A., Lennon, D. J., Kaufer, A., et al. 2001, ApJ, 547, 765. doi:10.1086/318424

Warren, S. J., Hambly, N. C., Dye, S., et al. 2007, MNRAS, 375, 213. doi:10.1111/j.1365-2966.2006.11284.x

Weiss, A. & Ferguson, J. W. 2009, A&A, 508, 1343. doi:10.1051/0004-6361/200912043

Whitelock, P. A., Menzies, J. W., Feast, M. W., et al. 2013, MNRAS, 428, 2216. doi:10.1093/mnras/sts188

Wright, E. L., Eisenhardt, P. R. M., Mainzer, A. K., et al. 2010, AJ, 140, 1868. doi:10.1088/0004-6256/140/6/1868

Zhang, S., Mackey, D., & Da Costa, G. S. 2021, MNRAS, 508, 2098. doi:10.1093/mnras/stab2642